



Strong Lens Models for 37 Clusters of Galaxies from the SDSS Giant Arcs Survey*

Keren Sharon¹, Matthew B. Bayliss², Håkon Dahle³, Samuel J. Dunham^{4,5}, Michael K. Florian⁶,
Michael D. Gladders^{7,8}, Traci L. Johnson¹, Guillaume Mahler¹, Rachel Paterno-Mahler⁹, Jane R. Rigby¹⁰,
Katherine E. Whitaker^{11,12}, Mohammad Akhshik¹¹, Benjamin P. Koester¹³, Katherine Murray¹⁴,
Juan David Remolina González¹, and Eva Wuyts¹⁵

¹ Department of Astronomy, University of Michigan, 1085 S. University Ave, Ann Arbor, MI 48109, USA; kerens@umich.edu

² Kavli Institute for Astrophysics & Space Research, Massachusetts Institute of Technology, 77 Massachusetts Ave., Cambridge, MA 02139, USA

³ Institute of Theoretical Astrophysics, University of Oslo, P.O. Box 1029, Blindern, NO-0315 Oslo, Norway

⁴ Department of Astronomy, Vanderbilt University, 6301 Stevenson Center Lane, Nashville, TN 37212, USA

⁵ Department of Physics and Astronomy, University of Tennessee, Knoxville, TN 37996, USA

⁶ Observational Cosmology Lab Code 665, NASA Goddard Space Flight Center, Greenbelt, MD 20771, USA

⁷ Department of Astronomy and Astrophysics, University of Chicago, 5640 South Ellis Avenue, Chicago, IL 60637, USA

⁸ Kavli Institute for Cosmological Physics, University of Chicago, 5640 South Ellis Avenue, Chicago, IL 60637, USA

⁹ University of California, Irvine, 4129 Frederick Reines Hall, Irvine, CA 92697, USA

¹⁰ Astrophysics Science Division, Goddard Space Flight Center, 8800 Greenbelt Rd., Greenbelt, MD 20771, USA

¹¹ Department of Physics, University of Connecticut, Storrs, CT 06269, USA

¹² Cosmic Dawn Center at the Niels Bohr Institute, University of Copenhagen and DTU-Space, Technical University of Denmark, Denmark

¹³ Department of Physics, University of Michigan, 540 Church St, Ann Arbor, MI 48109, USA

¹⁴ Space Telescope Science Institute, Baltimore, MD, USA

¹⁵ Armen TeKort Antwerp, Belgium

Received 2019 April 8; revised 2019 November 27; accepted 2019 December 2; published 2020 February 20

Abstract

We present strong gravitational lensing models for 37 galaxy clusters from the Sloan Digital Sky Survey Giant Arcs Survey. We combine data from multi-band *Hubble Space Telescope* Wide Field Camera 3 (WFC3) imaging, with ground-based imaging and spectroscopy from *Magellan*, Gemini, Apache Point Observatory, and the Multiple Mirror Telescope, in order to detect and spectroscopically confirm new multiply imaged lensed background sources behind the clusters. We report spectroscopic or photometric redshifts of sources in these fields, including cluster galaxies and background sources. Based on all available lensing evidence, we construct and present strong-lensing mass models for these galaxy clusters. The clusters span a redshift range of $0.176 < z < 0.66$ with a median redshift of $z = 0.45$, and sample a wide range of dynamical masses, $1.5 < M_{200} < 35 \times 10^{14} M_{\odot}$, as estimated from their velocity dispersions. As these clusters were selected as lenses primarily owing to a fortuitous alignment with background galaxies that results in giant arcs, they exhibit a wide range in Einstein radii, $1''.3 < \theta_E < 23''.1$ for a source at $z = 2$, with a median $\theta_E = 10''.8$. The reduced *HST* images and lens model outputs are made available to the scientific community as high-level data products with this publication.

Unified Astronomy Thesaurus concepts: Galaxy clusters (584); Strong gravitational lensing (1643); Gravitational lensing (670); Dark matter (353); Star-forming regions (1565); Observational astronomy (1145); High-redshift galaxies (734); Spectroscopy (1558)

Supporting material: machine-readable tables

1. Introduction

Strong-lensing models of galaxy clusters provide a detailed description of the mass distribution for the inner ~ 100 kpc. This method is complementary to other mass measurements, as it provides a high-resolution measurement of substructure at the core, on spatial scales at which other proxies such as X-ray, the Sunyaev–Zel’dovich (SZ) effect, dynamical masses, and weak lensing do not resolve.

In addition, the high magnification by clusters allows their use as “cosmic telescopes” to study background galaxies. Some of the highest redshift galaxies known were discovered as magnified sources in the fields of massive strong-lensing clusters (e.g., Zheng et al. 2012; Coe et al. 2013; Zitrin et al. 2014; Watson et al. 2015; Hashimoto et al. 2018; Salmon et al. 2018). At intermediate

redshifts, some of the best-studied star-forming galaxies are those that are magnified by gravitational lensing, which enables high signal-to-noise measurements (e.g., Petini et al. 2000, 2002; Cabanac et al. 2008; Quider et al. 2009, 2010; Dessauges-Zavadsky et al. 2011; Rigby et al. 2018a), and probes sub-galactic scales (e.g., Whitaker et al. 2014). Magnifications caused by the gravity of strong-lensing clusters can exceed factors of hundreds, if galaxies are fortuitously placed in close proximity to a lensing caustic.

To use galaxy clusters as telescopes, a detailed description of their mass distribution is key. The lens model determines the lensing magnification, which in turn connects the intrinsic and observed physical properties of the background sources: size, luminosity, star formation rate, and stellar mass. Thus, lens models are necessary in order to understand these lensed galaxies in the context of their source properties.

In the era of large optical surveys, the field of strong gravitational lensing is growing beyond detailed studies of a handful of strong-lensing clusters. Mining the Sloan Digital Sky Survey (SDSS) has yielded hundreds of new galaxy

* Based on observations made with the NASA/ESA *Hubble Space Telescope*, obtained at the Space Telescope Science Institute, which is operated by the Association of Universities for Research in Astronomy, Inc., under NASA contract NAS 5-26555. These observations are associated with programs GO-13003, GO-14622, GO-14230, GO-14896, GO-11974, GO-11100.

cluster-scale lenses, which form the SDSS Giant Arcs Survey (SGAS). Extensive follow-up observations of clusters from this survey included optical ground-based imaging and spectroscopy with a variety of telescopes, as well as two Large *Spitzer Space Telescope* programs. For some of these clusters there are X-ray and SZ observations. In a Large *Hubble Space Telescope* (*HST*) Guest Observer (GO) program, GO-13003 (hereafter SGAS-*HST*; PI Gladders), we obtained multi-band Wide Field Camera 3 (WFC3) images.

In this paper, we present strong gravitational lensing models of 37 galaxy clusters from SGAS, based on multi-band *HST* data and follow-up spectroscopy.

The *HST* subsample of SGAS, hereafter SGAS-*HST*, was designed to enable detailed study of the background highly magnified galaxies, most of which are observed at redshifts of $1 < z < 3$, the epoch when most of the stars in the Universe were formed (Madau & Dickinson 2014). These *HST* observations span a large wavelength range in order to sample the spectral energy distribution of each background galaxy. The high spatial resolution of *HST* reveals their morphology and stellar substructure, and combined with lensing magnification, probes sub-kiloparsec scales (e.g., Johnson et al. 2017a, 2017b; Rigby et al. 2017). The high spatial resolution of *HST* is critical for computing reliable lens models. It provides robust identification of images and counter-images of strongly lensed galaxies, and reveals additional lensed galaxies beyond the main (typically bright) source in each field.

This paper is organized as follows. In Section 2, we describe the SGAS; in Section 3 we present the *HST* imaging and the ground-based spectroscopy using the Gemini and *Magellan* telescopes; Section 4 describes the lens-modeling process in general, followed by cluster-specific lens model details, which are given in the subsections. We conclude in Section 6.

The reduced *HST* images and lens model outputs are made available to the scientific community as high-level data products with this publication via doi:10.17909/t9-cqtj-y020, on the Multimission Archive at the Space Telescope Science Institute (MAST).¹⁶

Throughout this work, unless specifically noted otherwise, we assume a flat cosmology with $\Omega_\Lambda = 0.7$, $\Omega_m = 0.3$, and $H_0 = 70 \text{ km s}^{-1} \text{ Mpc}^{-1}$. Magnitudes are reported in the AB system.

2. The Sloan Giant Arcs Survey

The SGAS is a survey for highly magnified galaxies that have been gravitationally lensed by foreground clusters of galaxies, in the SDSS (Blanton et al. 2017). The work presented here is based primarily on imaging and photometric catalogs from Data Release 7 (DR7; Abazajian et al. 2009). A full discussion of the survey, selection criteria, and purity and completeness estimate will appear in a separate paper (M. Gladders et al. 2020 in preparation). Galaxy clusters and groups were selected from the photometry catalog using the cluster red-sequence algorithm of Gladders & Yee (2000). Imaging data in g , r , i , and z were downloaded and cropped to 4.5×4.5 in size, centered on the detected clusters, with some overlap around larger clusters or filaments. The SDSS data were combined into color images, using a custom selection of scale and contrast in order to maximize the visual detectability of faint arc-like features. The color images were visually inspected by four investigators for

evidence of gravitational lensing. Each inspector scored each image on a scale of 0–3, where the highest score was given to obvious strong lenses. The process included a re-inspection rate of 10% of the images by each inspector in order to quantify the selection efficiency of each inspector, and the overall completeness of the sample. Candidate lenses were followed up by larger telescopes, with most of the confirmation done at the 2.56 m Nordic Optical Telescope. Spectroscopy of high-confidence arcs was obtained using Gemini North with the GMOS multi-slit spectrograph (Bayliss et al. 2011a, 2011b). All candidate lenses with an average score above 2 have been followed up in this way with 100% completeness; we reach 95% follow-up completeness for lens candidates with an average score between 1 and 2.

The multi-wavelength follow-up campaign of the SGAS sample includes imaging from space and ground: radio observations of the SZ Effect (Gralla et al. 2011), *Spitzer* infrared imaging (Program ID #90232, PI: Rigby; Program ID # 70154, PI: Gladders), wide field optical imaging for weak lensing with Subaru (Oguri et al. 2012), *HST* (GO-13003, PI: Gladders; see Section 3), UV imaging with SOAR (Bayliss 2012), and X-ray imaging with the X-ray telescope of the *Neil Gehrels Swift Observatory* (PI: Sharon) and *Chandra* (Program ID #19800436, PI: Bayliss). Spectroscopy of all the primary arcs is complete (Bayliss et al. 2011b), as well as spectroscopic campaigns to obtain redshifts of secondary arcs with *Magellan* (PI: Sharon) and Gemini (PI: Sharon; Johnson); see Section 3.2.

Since its initial assembly in 2008 (Hennawi et al. 2008), the SGAS sample of strong-lensing clusters has been mined for bright lensed galaxies that have been studied in detail (Bayliss et al. 2010, 2014b; Koester et al. 2010; Rigby et al. 2011, 2014, 2015, 2017; Wuyts et al. 2012a, 2012b; Dahle et al. 2013, 2015; Gladders et al. 2013; Johnson et al. 2017a, 2017b; Sharon et al. 2017; Chisholm et al. 2018). Many of the brightest lensed arcs from this program have high-quality rest-frame ultraviolet spectroscopy, obtained as part of MEGASURA (the *Magellan* Evolution of Galaxies Spectroscopic and Ultraviolet Reference Atlas; Rigby et al. 2018a). The study of these galaxies, which would otherwise be too faint for detailed spectroscopy, is only possible due to the magnification boost by the foreground cluster and fortuitous position of the background source in a region of highest magnification. The large sample of strong-lensing clusters also enabled research of the mass distributions of the galaxy clusters themselves (e.g., Gralla et al. 2011; Oguri et al. 2012; Blanchard et al. 2013; Sharon et al. 2014) and cosmic structure (Bayliss et al. 2011a, 2014a).

3. Observations

3.1. *HST* Imaging

The SGAS-*HST* program (GO-13003, PI: Gladders) consists of 107 orbits of *HST* imaging during Cycle 20. Each cluster was imaged with four WFC3 filters over three orbits. Table 1 details dates, filters, and exposure times of the *HST* observations. We supplement our observations with archival optical WFPC2 data from programs GO-11974 (PI: Allam) and GO-11100 (PI: Bradač), which were available for five fields. Subsequent *HST* programs of some of these targets acquired grism spectroscopy or additional bands, including GO-14622 (PI: Whitaker), GO-14230 (PI: Rigby), and GO-14896 (PI: Bayliss).

The GO-13003 observations were obtained with both the near-infrared (IR) and ultraviolet-visible (UVIS) channels of

¹⁶ <https://archive.stsci.edu/hlsp/sgas/>

Table 1
HST-GO-13003 Observations

Cluster	R.A. J2000	Decl. J2000	Date UT	Exposure Time (s)								
				F390W	F475W	F606W	F775W	F814W	F105W	F110W	F125W	F160W
SDSS J0004−0103	00:04:52	−01:03:15.80	2013 Sep 24	2388	2400	1112	1212
SDSS J0108+0624	01:08:42	+06:24:43.50	2013 Aug 3	2388	...	2400	1112	1212
SDSS J0146−0929	01:46:56	−09:29:52.40	2013 Sep 29	2388	...	2400	1112	1212
SDSS J0150+2725	01:50:01	+27:25:36.20	2013 Aug 2	2272	...	1456	...	1980	912
SDSS J0333−0651	03:33:05	−06:51:22.20	2013 Jul 17	2388	2400	1112	1212
SDSS J0851+3331	08:51:39	+33:31:10.83	2013 Feb 26	2368	2380	1112	1212
SDSS J0915+3826	09:15:39	+38:26:58.77	2013 Apr 3	2372	2388	1112	1212
SDSS J0928+2031	09:28:06	+20:31:25.55	2013 Feb 1	2388	...	2400	1112	...	1212
SDSS J0952+3434	09:52:40	+34:34:47.09	2013 Sep 28	2368	...	2380	1112	1112
SDSS J0957+0509	09:57:39	+05:09:31.80	2013 Mar 14	2388	2400	1112	1212
SDSS J1002+2031	10:02:27	+20:31:02.61	2013 May 15	2388	...	2400	1112	1212
SDSS J1038+4849	10:38:43	+48:49:18.73	2013 May 16	2392	1112	...	1212
SDSS J1050+0017	10:50:40	+00:17:06.91	2013 Apr 19	2388	...	2400	1112	...	1212
SDSS J1055+5547	10:55:05	+55:48:23.23	2013 Dec 7	2408	2424	1112	...	1212
SDSS J1110+6459	11:10:18	+64:59:47.02	2013 Jan 8	2420	...	2436	1112	1212
SDSS J1115+1645	11:15:04	+16:45:38.40	2013 Oct 28	2388	2400	1112	1212
SDSS J1138+2754	11:38:09	+27:54:30.90	2013 Mar 25	2384	2396	1112	1212
SDSS J1152+0930	11:52:47	+09:30:14.54	2013 May 17	2388	...	2400	1112	1212
SDSS J1152+3313	11:52:00	+33:13:41.72	2013 Jul 7	...	2380	2380	1112	...	1112
SDSS J1156+1911	11:56:06	+19:11:12.68	2012 Dec 4	2388	2400	1112	1212
SDSS J1207+5254	12:07:36	+52:54:58.20	2012 Nov 29	2400	...	2416	1112	1212
SDSS J1209+2640	12:09:24	+26:40:46.50	2013 May 5	2384	1112	1212
SDSS J1329+2243	13:29:34	+22:43:00.24	2013 May 16	2384	...	2400	1112	1212
SDSS J1336−0331	13:36:00	−03:31:28.63	2013 May 8	2388	...	2400	1112	1212
SDSS J1343+4155	13:43:33	+41:55:04.08	2013 Mar 13	2380	1112	1112
SDSS J1420+3955	14:20:39	+39:55:04.96	2013 Jan 17	2372	...	2388	1112	1112
SDSS J1439+1208	14:39:10	+12:08:24.75	2013 Jan 21	2384	2400	1112	1212
SDSS J1456+5702	14:56:01	+57:02:20.60	2013 Jan 10	2404	2424	1112	1212
SDSS J1522+2535	15:22:53	+25:35:29.36	2013 Jul 6	2384	...	2396	1112	1212
SDSS J1527+0652	15:27:45	+06:52:31.79	2013 Jan 16	...	2400	2400	1112	...	1212
SDSS J1531+3414	15:31:11	+34:14:24.91	2013 May 6	2256	...	1440	...	1964	912
SDSS J1604+2244	16:04:10	+22:44:16.69	2013 Jun 26	2384	2400	1112	...	1212
SDSS J1621+0607	16:21:32	+06:07:19.85	2013 Apr 29	2384	2400	1112	...	1212
SDSS J1632+3500	16:32:10	+35:00:30.16	2013 Oct 12	2372	2388	...	1112	...	1112
SDSS J1723+3411	17:23:36	+34:11:59.37	2013 Mar 14	2368	2380	1112	...	1112
SDSS J2111−0114	21:11:19	−01:14:23.57	2013 Jun 13	2388	1112	...	1212
SDSS J2243−0935	22:43:23	−09:35:21.40	2013 Aug 31	2388	...	2400	1112	1212
Typical point-source limiting magnitude (5σ)				26.39	26.38	26.11	25.65	25.49	25.85	26.17	25.81	25.66
Limiting magnitude uncertainty				±0.08	±0.03	±0.24	±0.23	±0.31	±0.22	±0.26	±0.31	±0.20

Note. Observing dates and exposure time of the clusters as part of *HST* program GO-13003. Columns 6 through 13 are the cumulative exposure times in each of the WFC3 filters, as labeled. Exposure times are in seconds. The limiting magnitudes are measured within a circular aperture of diameter $0''.7$.

the WFC3 instrument (Kimble et al. 2008) in order to minimize overheads. The primary science objective of GO-13003 is to measure the physical properties of the lensed galaxies. To accommodate that, the filter choice for each cluster was driven by the redshift of the primary arc, rather than the cluster redshift, for a long baseline rest-frame wavelength coverage with broad filters for maximal throughput. Each target was observed with the reddest filter available; the F160W on the IR camera. On the blue side, all but two clusters were imaged with the F390W filter on UVIS. The two intermediate bands were chosen to straddle the 4000 Å break at the redshift of the primary arc.

The observations using the two IR filters were executed within the same orbit, and data taken with the UVIS filters were executed in a single orbit each, all within one visit. In all cases, observations were split into four sub-exposures with sub-pixel dithers. The number of sub-exposures was found to be the minimum needed to sample the point-spread function (PSF), cover the chip gap, and enable removal of cosmic rays and other artifacts, while keeping to a minimum the readout noise and losses due to charge transfer efficiency (CTE). Targets were centered on the center of Chip 1 (UVIS) and with a channel pointing offset of +23''5 (IR) to optimally overlap the two fields of view, and avoid placing the center of the cluster on the chip gap. Where the visibility window allowed, we selected orientation angles that place the main arc in each cluster close to the readout side of the UVIS chip in order to minimize CTE losses in our primary science targets.

In the UVIS channel, the declining CTE of the detector can cause large flux losses and increases the correlated noise in the image. To mitigate, the bluest UVIS data were taken with post-flash, to increase the image background and ensure that faint sources have high enough counts (see WFC3 Data Handbook, Rajan 2010). Post-observation image corrections were applied to individual exposures using the Pixel-based Empirical CTE Correction Software¹⁷ provided by STScI.

The WFC3-IR observations were executed within a single orbit using a sampling interval parameter SPARS25, four images per filter with small box dithers for PSF reconstruction and to cover artifacts such as the “IR Blobs” and “Death Star” (WFC3 Data Handbook; Rajan 2010). We used a custom algorithm for a secondary correction of IR blobs that were not fully accounted for in the reduction pipeline of the WFC3-IR images as follows. We generated a superflat image from all the IR imaging in our program, and constructed an empirical model of the IR blobs using GALFIT (Peng et al. 2010). The IR blobs were then suppressed from individual exposures prior to drizzling, by dividing the data by the scaled model in a process similar to flat-fielding.

Individual corrected IR and UVIS images were combined using the AstroDrizzle package (Gonzaga et al. 2012) with a pixel scale of 0''.03 pixel⁻¹, and drop size of 0.5 for the IR filters and 0.8 for the UVIS filters. We find that this approach provides good recovery of the PSF in all bands and maximizes the sensitivity to low signal-to-noise features such as faint lensed galaxies. Finally, all images were drizzled onto the same pixel frame.

The typical point-source 5 σ magnitude limits of the entire survey are given in Table 1. We estimate the depth in each filter by randomly placing circular apertures with a diameter of 0''.7

across the PSF-matched images. We eliminate apertures that overlap with objects, and extract from the remaining background apertures the mean and standard deviation of the noise distribution for each field and filter. We next consider the distribution of depths for each filter. While the observing strategy was similar for most observations, different fields show some variation in their achieved depth, which is quantified as the standard deviation of the distribution (listed in Table 1).

3.2. Spectroscopy

Several different programs conducted spectroscopy of SGAS fields, using multiple observatories, with the science goal determining the observation strategy. These follow-up programs generally fall under two categories. The first type of programs includes multi-object spectroscopy using either a fiber-fed spectrograph or slit masks with multiple slits or slitlets placed primarily on arc candidates and cluster galaxies. Some of the results from these programs are published in Bayliss et al. (2011b, 2014a). With these observations, we secured new spectroscopic redshifts of lensed sources, and informed lens models and statistical analysis of the lensing cross section; spectroscopy of cluster-member galaxies were used to study the dynamical properties of the lensing clusters. The second type of spectroscopic program collects deep, high spectral resolution spectroscopy of individual lensed galaxies in order to study their physical properties, leveraging the high magnification by the foreground cluster (e.g., Wuyts et al. 2012a, 2012b; Bayliss et al. 2014b; Rigby et al. 2014, 2015, 2018a; M. Akhshik et al. 2020, in preparation; M. K. Florian et al. 2020, in preparation). Where available, we use results from these programs.

In this paper, we present new spectroscopic redshifts from Gemini and *Magellan* multi-slit spectroscopic programs. The primary goal of these programs was securing spectroscopic redshifts of secondary arcs in SGAS-*HST* fields. By construction of the *HST* target list, the primary arcs in each field already had secure spectroscopic redshifts. The secondary arcs have either not been identified prior to the *HST* observations, or previous attempts with *Magellan* or Gemini were unsuccessful at yielding redshifts. Spectroscopic redshifts of secondary arcs are critical for an accurate lens model, as the slope of the mass profile is degenerate with the distance of the lensed galaxies used as constraints. Redshifts of multiple source planes help break this degeneracy (e.g., Smith et al. 2009; Johnson & Sharon 2016). The secondary arcs are typically fainter than the primary arcs in each field. We therefore planned the observations to have longer exposures than previous SGAS programs (Bayliss et al. 2011b, 2014a). The observing strategy was optimized for securing spectroscopic redshifts of the background galaxies. Multi-object slit masks primarily targeted the lensing features around the cluster core. We placed additional slits on cluster-member galaxies and other objects of interest. The filters and gratings were selected to provide maximal wavelength coverage, to increase the redshift range in which redshifted emission lines can be observed.

Table 2 lists for each cluster the best available spectroscopic redshift, from the new observations described here, supplemented with information from previous programs including Bayliss et al. (2011b, 2014a), public databases (e.g., SDSS), and the literature. Where spectroscopic redshifts are available for several cluster-member galaxies, we define the cluster redshift as the mean redshift of these galaxies. Otherwise, the

¹⁷ http://www.stsci.edu/hst/wfc3/ins_performance/CTE/

Table 2
Cluster Properties

	Cluster	Redshift	σ_v (km s ⁻¹)	N_{spec}	M_{200} (10 ¹⁴ M _⊙)	Spectroscopy Reference	$\theta_E(z_s = 2)$ "
1	SDSS J0004-0103	0.514 ± 0.003	556 ± 178	9	1.5 ^{+1.9} _{-1.0}	Carrasco+17	3.9
2	SDSS J0108+0624	0.5478 ± 0.0002	...	1	...	SDSS DR12 BCG	2.3
3	SDSS J0146-0929	0.4469 ± 0.00006	...	1	...	SDSS DR12 BCG	12.4
4	SDSS J0150+2725	0.30619 ± 0.00005	...	1	...	SDSS DR12 BCG	12
5	SDSS J0333-0651	0.5729 ± 0.0006	...	1	...	BCG spectrum from APO/DIS	9.6
6	SDSS J0851+3331	0.3689 ± 0.0007	890 ± 130	41	6.6 ^{+3.3} _{-2.5}	Bayliss+14	16.4
7	SDSS J0915+3826	0.3961 ± 0.0008	960 ± 120	39	8.1 ^{+3.4} _{-2.7}	Bayliss+14	16.3
8	SDSS J0928+2031	0.192 ± 0.0009	965 ± 209	19	9.2 ^{+7.3} _{-4.8}	This work: GMOS, SDSS DR12	10.6
9	SDSS J0952+3434	0.357 ± 0.003	706 ± 214	10	3.3 ^{+4.0} _{-2.2}	This work: GMOS, SDSS DR12	10.9
10	SDSS J0957+0509	0.4482 ± 0.001	1250 ± 290	25	17.3 ^{+14.8} _{-9.4}	Bayliss+14	6.1
11	SDSS J1002+2031	0.319 ± 0.006	1110 ± 170	37	13.0 ^{+6.9} _{-5.1}	This work: GMOS, SDSS DR12	...
12	SDSS J1038+4849	0.4308 ± 0.0003	659 ± 69	48	2.6 ^{+0.9} _{-0.7}	Irwin+15, Bayliss+14	10.4
13	SDSS J1050+0017	0.5931 ± 0.0008	560 ± 80	32	1.5 ^{+0.7} _{-0.5}	Bayliss+14	15.4
14	SDSS J1055+5547	0.466 ± 0.003	678 ± 220	13	2.8 ^{+3.6} _{-1.9}	Bayliss+11	18.4
15	SDSS J1110+6459	0.656 ± 0.006	1022 ± 226	18	8.4 ^{+6.8} _{-4.4}	Johnson+17	10.1
16	SDSS J1115+1645	0.537	...	1	...	BCG spec Stark+13	8.6
17	SDSS J1138+2754	0.451 ± 0.008	1597 ± 380	11	35.7 ^{+31.7} _{-19.8}	Bayliss+11	15.6
18	SDSS J1152+0930	0.517 ± 0.009	1360 ± 320	6	21.3 ^{+18.6} _{-11.7}	Bayliss+11	6.6
19	SDSS J1152+3313	0.3612 ± 0.0007	800 ± 90	38	4.8 ^{+1.8} _{-1.4}	Bayliss+14	7.3
20	SDSS J1156+1911	0.54547 ± 0.00013	...	1	...	SDSS DR12 BCG	6.7
21	SDSS J1207+5254	0.275 ± 0.003	790 ± 410	4	4.9 ^{+12.0} _{-4.3}	SDSS DR12, Kubo+10	6.7
22	SDSS J1209+2640	0.5606 ± 0.0012	1155 ± 217	25	12.8 ^{+8.5} _{-5.9}	This work, Bayliss+11	22.7
23	SDSS J1329+2243	0.4427 ± 0.0007	830 ± 120	31	5.1 ^{+2.5} _{-1.9}	Bayliss+14	9.3
24	SDSS J1336-0331	0.17637 ± 0.00003	...	1	...	SDSS DR12 BCG	12.1
25	SDSS J1343+4155	0.418 ± 0.006	1011 ± 290	7	9.3 ^{+10.4} _{-5.9}	Bayliss+11	7.9
26	SDSS J1420+3955	0.607 ± 0.006	1095 ± 175	13	10.6 ^{+5.9} _{-4.3}	Bayliss+11	16.7
27	SDSS J1439+1208	0.42734 ± 0.00013	...	1	...	SDSS DR12 BCG	17.6
28	SDSS J1456+5702	0.484 ± 0.009	1536 ± 320	10	31.2 ^{+23.6} _{-15.6}	Bayliss+11	13
29	SDSS J1522+2535	0.602 ± 0.006	1187 ± 300	14	13.5 ^{+12.9} _{-7.8}	This work: GMOS, SDSS DR12	13.3
30	SDSS J1527+0652	0.392 ± 0.005	923 ± 233	14	7.2 ^{+6.9} _{-4.2}	Bayliss+11	1.4
31	SDSS J1531+3414	0.335 ± 0.005	998 ± 190	11	9.4 ^{+6.4} _{-4.4}	Bayliss+11	17.7
32	SDSS J1604+2244	0.286 ± 0.004	1042 ± 335	9	11.0 ^{+14.5} _{-7.6}	This work: GMOS, SDSS DR12	10.9
33	SDSS J1621+0607	0.3429 ± 0.0005	721 ± 97	48	3.6 ^{+1.6} _{-1.2}	This work, Bayliss+11	10.8
34	SDSS J1632+3500	0.466 ± 0.006	1212 ± 350	11	15.6 ^{+17.6} _{-9.9}	This work: GMOS, SDSS DR12	14.3
35	SDSS J1723+3411	0.44227 ± 0.00009	...	1	...	SDSS DR12 BCG	6.8
36	SDSS J2111-0114	0.6363 ± 0.0009	1090 ± 146	48	10.3 ^{+4.7} _{-3.6}	Bayliss+11, Carrasco+17	5.7
37	SDSS J2243-0935	0.447 ± 0.005	996 ± 200	20	8.8 ^{+6.4} _{-4.3}	Bayliss+11	23.1

Note. Spectroscopic redshifts, velocity dispersions, masses, and Einstein radii for the SGAS-*HST* lensing clusters. N_{spec} is the number of unique cluster-member galaxies with spectroscopic redshifts that were used to compute the velocity dispersion. We used the Gapper estimator for clusters with $N_{\text{spec}} < 15$ and the bi-weight sample variance otherwise (see Section 3.2). M_{200} masses were calculated from the velocity dispersions based on the scaling relations found by Evrard et al. (2008). References for spectroscopic redshift measurements of cluster galaxies are as follows: Carrasco et al. (2017), Bayliss et al. (2011b, 2014b), Irwin et al. (2015), Johnson et al. (2017b), Kubo et al. (2010), Stark et al. (2013). The last column lists the effective Einstein radii (θ_E) for a source at redshift $z_s = 2$, from the best-fit lens model derived by this work. θ_E is calculated as $\sqrt{A/\pi}$ where A is the area enclosed by the tangential critical curve.

redshift of the cluster is assumed to be the redshift of the brightest cluster galaxy (BCG). In our lensing analysis, the redshift of each cluster is taken to be known exactly without errors; the uncertainty has a negligible effect on the lensing analysis.

The velocity dispersion of each cluster is measured from all available spectroscopic redshifts. For clusters with a small number of galaxies with spectroscopic redshifts, $N_{\text{spec}} < 15$, we use the Gapper estimator (Beers et al. 1990). Otherwise, we use the square root of the bi-weight sample variance (Beers et al. 1990; Ruel et al. 2014). The uncertainties on the velocity dispersion are calculated as $\Delta\sigma_v = \pm 0.91\sigma_v/\sqrt{N_{\text{spec}} - 1}$, following Ruel et al. (2014). The velocity dispersions are listed in Table 2.

The dynamical masses are given for reference, and are calculated from the velocity dispersions based on the scaling relations found by Evrard et al. (2008).

3.2.1. Gemini/GMOS-North Spectroscopy

Spectroscopic observations of SGAS clusters were obtained using the Gemini North telescope as part of programs GN-2015A-Q-38 (PI: Sharon) and GN-2015B-Q-26 (PI: Sharon) using the Gemini Multi-Object Spectrograph (GMOS; Hook et al. 2004).

All Gemini/GMOS-North observations were conducted in queue mode using the R400_G5305 grating in first order and

Table 3
Summary of Spectroscopic Observations

Cluster	Telescope/Instrument	UT Date	Exposure Time	Program ID
SDSS J0851+3331	Gemini/GMOS-North	2015 Apr 18	2 × 2400 s	GN-2015A-Q-38
SDSS J0928+2031	Gemini/GMOS-North	2015 Apr 18,19	2 × 2400 s	GN-2015A-Q-38
SDSS J0952+3434	Gemini/GMOS-North	2015 Oct 23, 2016 Jan 3	2 × 2880 s	GN-2015B-Q-26
SDSS J1002+2031	Gemini/GMOS-North	2016 Jan 4, 7	2 × 2880 s	GN-2015B-Q-26
SDSS J1002+2031	Gemini/GMOS-North	2011 May 22	2 × 2400 s	GN-2011A-Q-19
SDSS J1110+6459	Gemini/GMOS-North	2016 Jan 8	2 × 2880 s	GN-2015B-Q-26
SDSS J1207+5254	Gemini/GMOS-North	2016 Feb 4	2 × 2880 s	GN-2015B-Q-26
SDSS J1209+2640	Gemini/GMOS-North	2016 Feb 9	2 × 2880 s	GN-2015B-Q-26
SDSS J1329+2243	Gemini/GMOS-North	2011 Jun 2	2 × 2400 s	GN-2011A-Q-19
SDSS J1604+2244	Gemini/GMOS-North	2011 Apr 29	2 × 2400 s	GN-2011A-Q-19
SDSS J1602+3500	Gemini/GMOS-North	2012 Apr 15	2 × 2400 s	GN-2011A-Q-19
SDSS J0146−0929	Magellan/IMACS MOS	2013 Nov 6	3 × 2400 s	...
SDSS J0150+2725	Magellan/IMACS MOS	2013 Mar 16	6 × 2400 s (2 masks)	...
SDSS J1152+0930	Magellan/IMACS MOS	2014 Apr 24, 25, 26	10 × 2400 s (2 masks)	...
SDSS J1336−0331	Magellan/IMACS MOS	2013 Jul 11, 2014 Apr 24	10 × 2400 s (2 masks)	...
SDSS J1336−0331	Magellan/LDSS3 long-slit	2013 May 2	2400 s	...
SDSS J1439+1208	Magellan/IMACS MOS	2014 Apr 26	2 × 2400+3300 s	...
SDSS J1439+1208	Magellan/IMACS long-slit	2013 Mar 17	2 × 1200 s	...
SDSS J1621+0607	Magellan/IMACS MOS	2013 Aug 3	3 × 2400 s	...
		2014 Apr 24, 25, 26	2 × 3000, 2 × 2880, 2 × 2700 s	...
SDSS J1621+0607	Magellan/LDSS3 long-slit	2013 May 2	1800+2400 s	...
SDSS J2111−0114	Magellan/IMACS MOS	2013 Aug 2, 3, 2014 Apr 24,25	2 × 3600, 6 × 2400 s	...
SDSS J2243−0935	Magellan/IMACS MOS	2013 Jul 11, 2013 Nov 6, 7	4 × 2400 s	...
SDSS J0333−0651	Magellan/FIRE	2013 Mar 1	2400 s	...
SDSS J0928+2031	Magellan/FIRE	2013 Feb 28	2400 s	...
SDSS J1439+1208	Magellan/FIRE	2013 Feb 28	9600 s	...
SDSS J0108+0624	APO/DIS	2012 Jan 20	2 × 1200 s	...
SDSS J0150+2725	APO/DIS	2012 Jan 20	2 × 3000 s	...
SDSS J1456+5702	MMT/Blue Channel	2014 May 4	2 × 1200 s	...

Note. Spectroscopic observation dates and exposure times. UT date lists the date or dates of the observation. Number of exposures and integration time of each exposure are listed in the fourth column. Magellan observations are typically split over two or more sub-exposures. Program ID lists the proposal identifier in the Gemini archive.

the G515_G0306 long pass filter. Table 3 lists the observation dates and exposure times for the clusters that were targeted in these programs. We designed one multi-object slit mask for each cluster, placing slits on the high priority secondary arcs in each cluster for which spectroscopic redshifts had not been previously measured. Other slits were placed on cluster galaxies, selected by their color relative to the cluster red sequence.

We also report redshifts from program GN-2011A-Q-11 (PI: Gladders) of primary arcs and cluster members that were not published elsewhere. Those observations, as well as the data reduction procedures of the GMOS data, are described in Bayliss et al. (2014a).

3.2.2. Magellan Spectroscopy

We followed up clusters that are observable from the south, with decl. $<20^\circ$, with the *Magellan* 6.5 m telescopes at Las Campanas Observatory, Chile. As with the Gemini observations described in the previous section, we obtained spectra of secondary arcs that were identified in the *HST* data, and not targeted by Bayliss et al. (2011b). We observed eight cluster fields with the Inamori-Magellan Areal Camera & Spectrograph (IMACS) on the Baade telescope, using multi-slit spectroscopy. We designed one or two

masks per field, placing $1''.0$ slitlets on the lensed galaxies at highest priority, and filling the rest of the $27''.2 \times 27''.2$ field of view with cluster-member galaxies and other sources. We observed one cluster field with $1''.0$ long-slit. Observations were typically several exposures of 2400 s each.

We report redshifts in two cluster fields that we observed with the Low Dispersion Survey Spectrograph 3 (LDSS3) camera on the Clay telescope using either the $1''.0$ or $1''.5$ long slit.

We report new redshift measurements in three fields: SDSS J0333−0651, SDSS J0928+2031, and SDSS J1439+1208, using the Folded-port InfraRed Echellette (FIRE) on the Baade telescope. The observations took place on 2013 March 1 with clear weather conditions and $0''.7$ seeing. We used the Eschelle disperser with $1''.0$ slit, typically integrating for 40 minutes.

3.2.3. Apache Point Observatory Spectroscopy

Observations with the Dual Imaging Spectrograph (DIS) on the 3.5 m telescope at Apache Point Observatory (APO) on 2012 January 20 were used to measure the redshifts of two arcs in this paper. The observation strategy and data reduction procedures are identical to those detailed in Bayliss (2012).

3.2.4. Multiple Mirror Telescope Observatory Spectroscopy

Observations with the 6.5 m Multiple Mirror Telescope (MMT) using the Blue Channel spectrograph were obtained on 2014 May 4 (PI: Bayliss) for one of the targets in this paper, the giant arc in SDSS J1456+5702. We used the 500 line grating in first order, tilted to set the central wavelength to 5575 Å, using the 1.25 wide long-slit aperture at a position angle (PA) of 87.3 east of north. The source was at airmasses between 1.18 and 1.38 during the science exposures, and conditions remained clear with consistently subarcsecond seeing. The science frames were followed by HeNeAr arc lamp wavelength calibration frames and quartz lamp flat calibration frames taken at the same PA. We bias-subtracted, flat-field corrected, and wavelength calibrated the data with standard IRAF routines in the `iraf.noao.imred.ccdred` and `iraf.noao.onedspec` packages. We then used custom IDL code built using the XIDL package to subtract a two-dimensional model of the sky on a pixel-by-pixel basis. The science spectrum was boxcar extracted to capture from the full extended object profile of the giant arc along the slit, using a 3" wide aperture. The final combined spectrum covers a range in wavelength of $\sim 4000\text{--}7175$ Å, with a dispersion of 1.19 Å per pixel and a median spectral resolution, $R = \delta\lambda/\lambda \simeq 1150$.

4. Strong-lensing Analysis

We compute strong-lensing models using the public software `Lenstool` (Jullo et al. 2007). `Lenstool` assumes a “parametric” solution to describe the mass distribution, and solves for the best-fit set of parameters using Markov Chain Monte Carlo (MCMC) sampling of the parameter space. The best-fit model is defined as the one that results in the smallest scatter between observed and model-predicted image positions in the image plane.

We model each cluster as a linear combination of mass halos, representing the dark matter mass distribution attributed to the cluster and to correlated large scale structure, and individual cluster galaxies. The halos are modeled as pseudo-isothermal ellipsoidal mass distribution (PIEMD, also known as dPIE; Jullo et al. 2007), with seven parameters: position x, y ; ellipticity e ; position angle θ ; core radius r_{core} ; cut radius r_{cut} ; and a normalization σ_0 . We note that σ_0 , the effective velocity dispersion, is correlated with, but not identical to, the observed velocity dispersion of the mass halo. The relation to the observed velocity dispersion, σ_v , can be found in Elíasdóttir et al. (2007) for the PIEMD potential. The two mass slope parameters, r_{core} and r_{cut} , define an intermediate region $r_{\text{core}} \lesssim r \lesssim r_{\text{cut}}$ within which the mass distribution is isothermal; the potential transitions smoothly to a flat profile toward $r = 0$, and asymptotes to zero at large radii.

The normalization and radii parameters of the galaxy-scale halos are scaled to their observed luminosity (see Limousin et al. 2005 for a description of the scaling relations). The positional parameters (x, y, e, θ) are fixed to their observed measurements, as measured with Source Extractor (Bertin & Arnouts 1996).

Unless noted otherwise, all the parameters of cluster-scale halos are allowed to vary, with the exception of r_{cut} , which is far outside the strong-lensing region and thus cannot be constrained by the lensing evidence. We therefore fix this parameter at 1500 kpc.

We estimate the statistical uncertainties on individual model parameters from the MCMC sampling of the parameter space. These uncertainties do not include systematic uncertainties due to modeling choices, structure along the line of sight, or correlated structure and substructure, which have been shown to cause systematic uncertainties (e.g., Zitrin et al. 2015; Acebron et al. 2017; Johnson et al. 2017b; Meneghetti et al. 2017; Prieve et al. 2017; Cerny et al. 2018). From the lensing potential we compute the mass distribution, convergence, shear, magnification, and deflection maps. We refer the reader to Johnson et al. (2014) for a concise description of these derivatives, and their dependence on the cluster and source distances. We estimate the statistical uncertainties of these lensing outputs by computing a suite of models sampled from the MCMC chain.

4.1. Identification of Cluster Galaxies

Cluster members are identified as forming a tight ridge in color–magnitude diagrams, often referred to as “red sequence” (e.g., Gladders & Yee 2000; Koester et al. 2007). The color of the red sequence depends on the cluster redshift and the selection of filters. We note that some fraction of the galaxy population is not quiescent (Butcher & Oemler 1978, 1984), and thus the red-sequence method forms an incomplete cluster-member selection. However, this fraction decreases significantly in the inner 1 Mpc (e.g., Fairley et al. 2002; Bai et al. 2007; Loh et al. 2008; Porter et al. 2008; Saintonge et al. 2008; Hansen et al. 2009). In cases where the lensing signal is clearly affected by individual galaxies, even when they are not on the red sequence, we include these galaxies in the model.

4.2. Lensed Sources

The SGAS clusters were selected based on visual inspection of SDSS images of lines of sight toward galaxy clusters. Therefore, by construction of the sample, each cluster has at least one bright arc detectable with shallow ground-based imaging. Deeper follow-up provided a multitude of fainter arc candidates, some of which were confirmed by spectroscopy (Bayliss et al. 2011b). In optical bands, the depth of the *HST* imaging does not exceed that of the ground data; however, the excellent resolution allows us, in most cases, to unambiguously identify multiple images, detect substructure in extended arcs, and discriminate among arc candidates. The deep *HST* near-IR imaging provides wide wavelength coverage with a lever arm on color variance, and a window to the high-redshift universe as well as highly extinguished star-forming galaxies. In discovering new arc candidates, we are often assisted by the preliminary lens model, which is based on the primary arc and other known lensed galaxies. The initial model is often successful in predicting the approximate location of possible counter-images. This is typical for lens models that assume some form of correlation between the mass distribution and the light of cluster galaxies (e.g., Broadhurst et al. 2005). We note that this process of using an initial model to aid in the discovery of new arcs is not limited to mass-follows-light models; fully parametric models such as `Lenstool` can provide good initial guesses. Following the recommendations of Johnson & Sharon (2016), each time a lensed source was spectroscopically confirmed, we reassessed any images with no spectroscopic confirmation that have been predicted by the lens model before adding them back in as lensing constraints.

In some cases, we use information from photometric redshift analysis of lensed galaxies as a prior. Photometric redshifts were derived using the EAZY code (Brammer et al. 2008), which fits linear combinations of seven templates to the broadband spectral energy distributions that span a broad range of galaxy colors while minimizing color and redshift degeneracies. A K -band apparent magnitude prior and systematic errors due to template mismatch are taken into account, following (Whitaker et al. 2011).

Owing to the superior resolution of *HST* and the broader wavelength coverage compared to the previous ground-based data, we discovered new arc candidates in most of the cluster fields. These are presented in Tables 4–10, with coordinates, IDs, and where available, spectroscopic or photometric redshifts.

4.3. Lensing Analysis of Individual Clusters

In this section, we provide details on the identification of lensed sources and modeling choices for each cluster in this *HST* program. The ability to construct a unique, high-fidelity, lens model varies from cluster to cluster, and is dominated by the availability of lensing constraints, availability of spectroscopic redshifts, and other factors that are less straightforward to quantify such as the distribution of lensing constraints in the field of view. Numerical estimators that are often used for assessing models, such as χ^2 , reduced χ^2 , and rms, may be good indicators of the statistical errors in the parameter space, but do not necessarily encompass the full uncertainty (e.g., Johnson & Sharon 2016; Cerny et al. 2018). We therefore resort to providing a subjective assessment of the reliability of each model as a well-understood cosmic telescope. We rate the lens models in three broad categories: Category *A* denotes a high-quality, robust model, whose magnification is relatively well constrained; in category *B* we place acceptable models, with somewhat higher systematic uncertainties; and *C* denotes poor models, that are underconstrained. Models that fall at the top or bottom of these quality bins are denoted with + or –, respectively. We indicate below the caveats and point to sources of uncertainty for individual cluster models if they significantly reduce the reliability of the model, i.e., fall in category *B* or *C*.

Tables 4–10 list the lensing constraints in each field, which are described in the subsections below. We tabulate the IDs, coordinates, and redshifts of the lensed galaxies, as well as individual emission knots within the lensed galaxies that were used as constraints. The IDs appear as *ABX* where *A* is a number or a letter indicating the source ID (or system name); for images with identified substructure, *B* is a number or a letter indicating the ID of the emission knot within the system; and *X* is a number indicating the ID of the lensed image within the multiple-image family. For example, 1a.3 would be the third image of emission knot *a* in system #1. Images without clearly identified substructure would appear as *A.X*. In a few cases, we retain the naming systems that were used in previous publications.

In Figures 1 through 7, we present the 37 clusters in this program. The images are rendered from three of the *HST* bands as noted in the bottom-left corner of each panel. The clusters are shown in order of R.A., and their names are shown on the top left. The field of view of each panel is selected in order to best show the strong-lensing region; we plot a 5'' scale bar at the bottom-right corner of each panel. The critical curves are overplotted in red, representing the loci of maximum

magnification for a source at redshift z , as indicated in the bottom left of each panel. We plot the locations of the observed lensed galaxies. Each family is labeled in the same color; for clarity, we do not label multiple knots within the lensed images; they are given in Tables 4–10. Finally, spectroscopic redshifts are listed at the top-right corner of each panel, with the same color code. For completeness, we list spectroscopic redshifts of sources even if they fall outside of the field of view of the panel.

4.3.1. SDSS J0004–0103

The *HST* imaging confirms the bright arc that was previously discovered in ground-based data. The *HST* resolution reveals the clumpy morphology of this arc. We identify several distinct emission knots, and determine that the arc consists of three merging partial images of the background source. We use individual emission clumps as lensing constraints. The cluster itself is diffuse, with no obvious dominant galaxy at its core. We use the Gapper estimator to calculate the velocity dispersion from spectroscopic redshifts of nine cluster galaxies measured by Carrasco et al. (2017), $\sigma_v = 556 \pm 178 \text{ km s}^{-1}$. This velocity dispersion is consistent with a small group rather than a rich cluster. We use the velocity dispersion as an upper limit on the lensing mass distribution when computing the lens model.

Due to the limited lensing constraints and the uncertainty of where the cluster center is, the lens model is not unique and has large systematic uncertainty. We rank its fidelity for predicting the magnification anywhere in the field and its ability to constrain the mass distribution as *C* (poor, underconstrained). At the same time, the model is successful at reconstructing the morphology and geometry of the lensed source and explaining the lensing configuration, and can be used to place limits on the magnification of the lensed galaxy.

4.3.2. SDSS J0108+0624

We confirm the identification of one bright arc, at a projected angular distance 3''.3 from the BCG, at $z_{\text{spec}} = 1.91$ (Rigby et al. 2018b). The *HST* data reveal a demagnified counter image separated 0''.52 from the BCG. We also identify several bright emission knots, color variation along the magnified arc, and clumpy morphology in both images, which helps constrain the lens model. No additional lensed galaxies were identified. The internal morphology and color variation along the giant arc indicate that this is a system of two images, with the giant arc being one complete image of the source, and the demagnified central image the second image. A third image is predicted behind the central cluster galaxy. We observe faint F390W emission at this location. However, as some of the other cluster members show faint emission in this filter at their centers as well, the data cannot rule out that this emission is coming from the central cluster galaxy. This model is not as well constrained as others in this sample, as the constraints come from a single lensed galaxy with only two images. Since the lens is dominated by a central galaxy and the identification of the central image provides a good constraint on the center of the lens, the model is of sufficient fidelity for measuring the mass distribution in the core. However, we place it in category *B* due to the high uncertainty on the lensing magnification.

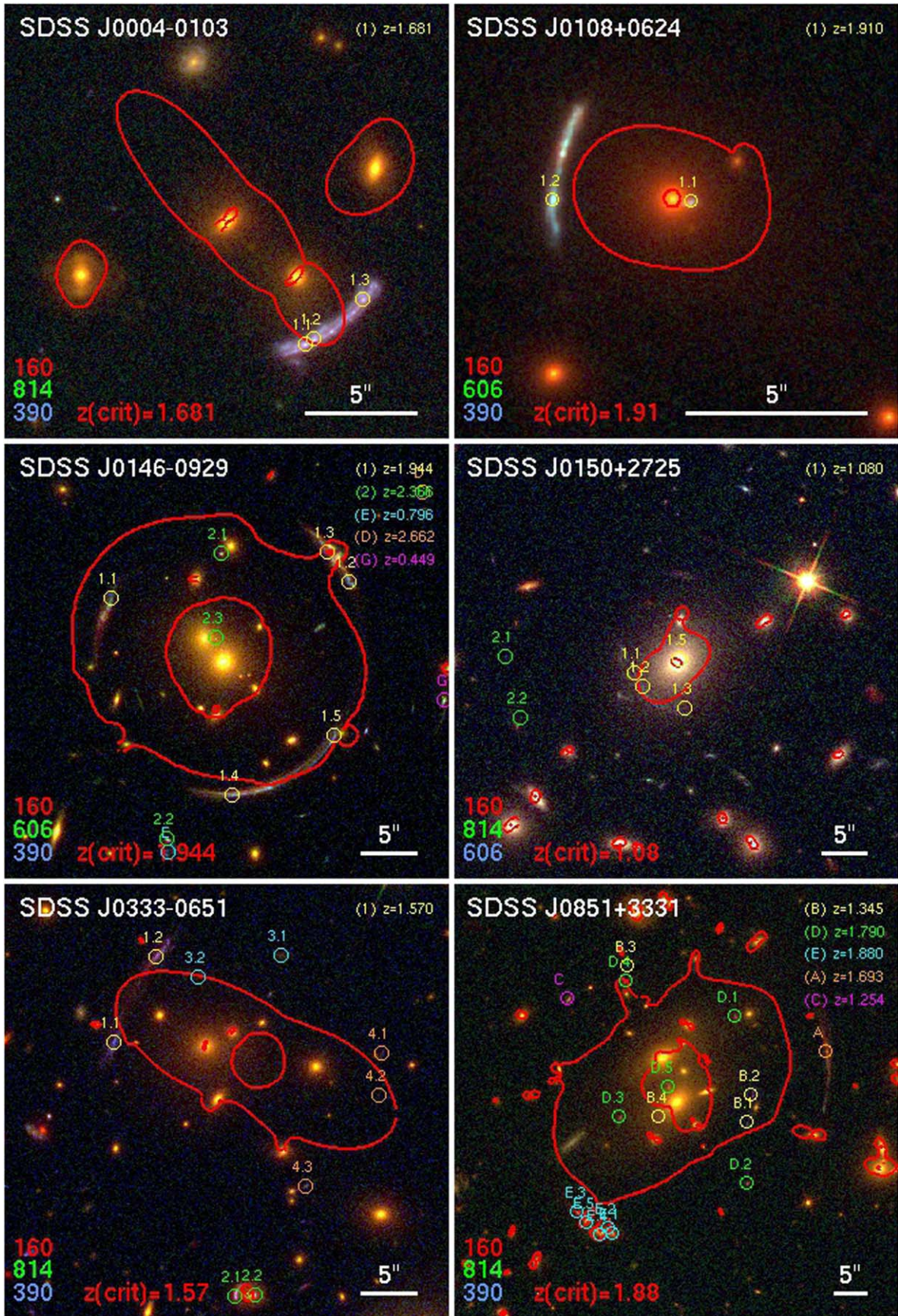


Figure 1. Composite color images of the SGAS-HST clusters SDSS J0004–0103, SDSS J0108+0624, SDSS J0146–0929, SDSS J0150+2725, SDSS J0333–0651, and SDSS J0851+3331. North is up and east is left in all panels. The images are from the *HST* bands that best show the lensed galaxies, with the filters noted in the bottom-left corner of each panel. The coordinates, redshifts, and references are tabulated in Table 4.

4.3.3. SDSS J0146–0929

The primary source lensed by SDSS J0146–0929 appears as an incomplete Einstein ring around the BCG, with a mean projected radius of $12''.1$. The *HST* resolution reveals morphology and color variation along the lensed galaxy. We identify image 1.1 (northeast of the BCG) to be a complete image of the source. The arc that appears to the south of the BCG is a merging pair of two partial images of the source, which we label 1.4 and 1.5. The arc northwest of the BCG is affected by the lensing potential of two interloper galaxies, likely cluster members, leading to a complex critical curve at this location and breaking up this arc into two partial images 1.2 and 1.3 (the “main” arc) and additional partial images buried in the light of the interlopers. We use several emission clumps in the source as constraints. The spectroscopic redshift of this galaxy was reported by Stark et al. (2013). We identify and spectroscopically confirm a second lensed galaxy with two secure images, 2.1 and 2.2. One image was predicted by the lens model near the center of the cluster. We identify a likely candidate, but it is not used as a constraint.

We obtained multi-slit spectroscopy from *Magellan* on 2013 Nov 6, using IMACS on the Baade telescope (Table 11). From these data, we measured the redshift of source #2, $z_{\text{spec}} = 2.366$, from [C III] 1907, C III] 1909 Å. The other background sources with spectroscopic redshifts that are listed in Table 11 are likely not strongly lensed (i.e., we do not expect them to have counter-images). The model is well represented by a central cluster-scale halo and cluster-member galaxies. We leave the slope parameters of the two galaxies near the northwest arc as free parameters, and fix their positional parameters to their observed values. The lens model is well constrained, and we classify it in category A.

4.3.4. SDSS J0150+2725

The main arc in this field is a low surface brightness galaxy at $z_{\text{spec}} = 1.08$, measured from the [O II] 3727, 3729 Å line in spectroscopy from the 3.5 m telescope at the APO, obtained on 2012 January 20, with the APO/DIS instrument. Although some candidates were suggested from ground data, a careful inspection of the *HST* images shows that their morphology or color are not the same and thus we rule them out as strongly lensed systems. We identify a counter image of the giant arc very close to the central galaxies, embedded in the BCG light. However, the distinct blue color of this galaxy gives it a high contrast against the cluster galaxies, which are mostly dropped out of our bluest band (F390W). We also identify two faint images of a candidate lensed galaxy. A third image is predicted, but would be less magnified and fall under our detection limit. The lensing constraints are sufficient for a robust model, however, due to the lack of spectroscopic redshift for source #2 the slope of the mass distribution is not well constrained. We therefore classify the model in category B (acceptable with higher uncertainty).

4.3.5. SDSS J0333–0651

The giant arc in this field, source # 1 at $z_{\text{spec}} = 1.57$, was spectroscopically confirmed with *Magellan*/FIRE observation obtained on 2013 March 1. It is likely a single, highly distorted and flexured lensed galaxy. It appears resolved in the *HST* data; however, its substructure and color variation do not show lensing symmetry. We identify one secure lensed source, likely a galaxy–galaxy lensing event forming a partial Einstein ring around an elliptical galaxy $22''.2$ south of the BCG (close to the

bottom of Figure 1). We have no spectroscopic data for this source. We further identify two other candidate lensed systems, labeled 3 and 4.

Due to the limited strong-lensing constraints, the lens model for this cluster is less robust than other clusters in our program. We therefore classify it as B+. Spectroscopic redshifts of sources #3 and #4 would strengthen the model, as well as deeper observations to identify additional (fainter) images that are expected to occur for system #3. Alternatively, if no further constraints are revealed, future analysis may use the flexion (curved distortion due to the third derivatives of the lensing potential) of the main arc as a constraint to improve the fidelity of the model (e.g., Cain et al. 2016). Flexion constraints are currently not implemented in the lens-modeling algorithm we use.

4.3.6. SDSS J0851+3331

This cluster lenses a few background sources, some of which were identified by Bayliss et al. (2011b). Source A at $z_{\text{spec}} = 1.6926$ (Bayliss et al. 2011b, labeled A1 and A2), appears as a highly stretched and flexured arc, with significant color gradient, and is a single image. The two images of source B that were identified and measured by Bayliss et al. (2011b), labeled B.1, B.2 at $z_{\text{spec}} = 1.3454$, have matching morphology in the *HST* imaging, with the expected lensing symmetry. We identify two new counter-images for this source, B.3 and B.4, for a total of four images of the lensed source. Source C is a single image. We identify two new lensed systems in the *HST* data: source D has five images around the center of the cluster, with spectroscopic redshift $z_{\text{spec}} = 1.79$, measured from *HST*-WFC3-IR grism spectroscopy with *HST* (GO-14622, PI: Whitaker). Source E has four secure images, and is brightest in the infrared bands. The lensing configuration of the images of source E is dominated by two cluster galaxies $\sim 20''$ south of the BCG. A candidate partial fifth image is identified. This source was the science target of GO-14622, which measured a spectroscopic redshift $z_{\text{spec}} = 1.88$, confirming the photometric redshift that we initially inferred based on *Spitzer* observations and the *HST* data presented here. An analysis of this source will be presented in a forthcoming publication (M. Akhshik et al. 2020, in preparation). Given the number, quality, and distribution of constraints, the model is of high fidelity, and we classify it in category A.

4.3.7. SDSS J0915+3826

This cluster was previously modeled by Bayliss et al. (2010) based on ground-based data. That work identified two lensed sources, and measured their redshifts: source A at $z_{\text{spec}} = 1.501$ and source B, a Ly α -emitting galaxy at $z_{\text{spec}} = 5.2$. Our new *HST* imaging confirm the interpretation of these images as lensed galaxies. Furthermore, with the *HST* resolution we pin down the lensing morphology of the giant arc and determine that it is made of three merging images of the source galaxy. Several emission knots are clearly identified within the galaxy. For source B, Bayliss et al. (2010) were unable to identify a counter image, and therefore this source was not used as a constraint. Our *HST* data help reveal two counter-images with the same unique color as source B, enabling its use as lensing constraint. Lensing potential from a nearby cluster-member galaxy perturbs the critical curve at the location of B.1. The model is of high fidelity, and we classify it in category A.

4.3.8. SDSS J0928+2031

The distribution of cluster-member galaxies and the lensing evidence in this field suggest that SDSS J0928+2031 is composed of two subhalos, each dominated by a bright elliptical galaxy. The northwest halo appears to be the more massive, based on the lensing evidence and its appearance in archival *Chandra* data. This cluster was selected as a strong lens based on an identification of an elongated arc north of the BCG, labeled 1 in Figure 2. The giant arc likely forms along the critical curve for its redshift, with a bright knot falling just outside of the caustic and thus not multiply imaged. We identify several additional lensing constraints near the northwest core of the cluster. Spectroscopy was obtained with the *Magellan* Clay telescope using FIRE on 2013 February 28, securing spectroscopic redshifts of the main arc at $z_{\text{spec}} = 1.891$, and of two other sources that are likely not multiply imaged (Table 11). We note a group of red galaxies near source C, which appear to be low-redshift dusty galaxies; while their FIRE spectra did not have high enough signal-to-noise for a high-confidence redshift, their *Spitzer* luminosity and optical colors are similar to those of source C, and the spectra are consistent with $z \sim 1.9$. We obtained multi-slit spectroscopy from Gemini North as part of program GN15AQ38 (PI: Sharon), and measured spectroscopic redshifts of arc candidates 2 and 3 and cluster-member galaxies (see Tables 5, 11, respectively).

The second bright galaxy in this cluster lies $46''$ southeast of the BCG in projection. We identify a flexured galaxy at $z_{\text{spec}} = 0.856$ northwest of the galaxy, in the direction of the BCG. No counter-images are identified for this galaxy, and it is likely in the strong-weak lensing regime rather than strongly lensed. We identify a candidate radial arc, system 5, and use it as a constraint in the south halo. The lack of strong-lensing constraints prevents us from robustly modeling the mass distribution that may be attributed to a possible dark matter clump in the south region. The projected mass density implied from the model is consistent with the velocity dispersion, which we measured from 15 galaxies we observed with GMOS and four galaxies from SDSS DR12. The model therefore provides a reliable description of the mass and magnification around the northwest core (category A), from multiple lensing constraints and source redshifts around its core; but it is underconstrained in the area surrounding the southeast core (category C).

4.3.9. SDSS J0952+3434

A giant arc is observed south of the cluster core ($z_{\text{spec}} = 2.1896$, Kubo et al. 2010). The giant arc does not show particular symmetry, and we do not robustly identify a counter image. We identify tentative faint multiple images of other sources that can be used to constrain the lens model. However, the low confidence with which they are identified, and the lack of confirmation of a counter image for the giant arc, results in a low-confidence lens model (category B). The lens model, the loose appearance of the galaxy distribution, and overall density of galaxies, are consistent with the low projected velocity dispersion we calculate for this cluster (Table 2) from spectroscopic redshifts of eight cluster-member galaxies from Gemini/GMOS and two galaxies with spectra in SDSS DR12 (Table 11).

4.3.10. SDSS J0957+0509

The *HST* data show that the giant arc of source 1 in SDSS J0957+0509 is composed of several merging images of a single background galaxy. Cluster-member galaxies that are in close projected proximity to the arc contribute to a complex lensing configuration. We identify five bright images within the giant arc, and one faint demagnified image near the center of a galaxy $7''.8$ west of the BCG. The redshift of this source was measured by Bayliss et al. (2011b), $z_{\text{spec}} = 1.821$. In addition to the giant arc, we identify two other lensed systems in the *HST* data, #2, #3. Each of these systems has four visible images, with a fifth demagnified image predicted by the lens model near the center of the BCG. The lens model is reliable, and we classify it as A-. Securing spectroscopic redshifts for sources #2 and #3 would add confidence to the model that is otherwise well constrained.

4.3.11. SDSS J1002+2031

Ground-based imaging of this cluster show an obvious giant arc, located $14''.0$ west of the BCG, labeled #1 in Figure 2. A second elongated feature appears bright in red/infrared bands, $18''.1$ west of the BCG, labeled A in Figure 2. Using our *HST* imaging data, we identify a tentative candidate counter image for the giant arc (labeled #1.2). The red feature, which also looks like an elongated arc from the ground, appears as two galaxies in the *HST* data. It does not have a counter image, and is likely a magnified single image. We do not identify other strong-lensing constraints in the data. We observed this field using GMOS on Gemini North (GN11AQ19 and GN15BQ26) and obtained spectroscopic redshifts of background galaxies and cluster-member galaxies. The spectroscopy places the blue giant arc at $z_{\text{spec}} = 0.985$, and galaxy A that was initially identified as a red arc at $z_{\text{spec}} = 1.27$. Another bright background galaxy, C, is found $26''.1$ east of the BCG, with spectroscopic redshift $z_{\text{spec}} = 0.734$. These two spectroscopically confirmed, singly imaged galaxies help in constraining possible lens models, as we can rule out models that predict counter-images for these galaxies. Nevertheless, we find that these constraints are not sufficient for a robust lens model. This model is therefore classified as C- (poor, underconstrained). The dashed critical curve that is shown in Figure 2 represents a family of models that is capable of reproducing the lensing geometry of the blue arc; however, these models are likely incorrect because they predict counter-images for galaxy A.

4.3.12. SDSS J1038+4849

As can be seen in Figure 2, there are several giant arcs with large azimuthal coverage around the cluster core. Bayliss et al. (2011b) measured spectroscopic redshifts of four unique sources (see Table 5). The new *HST* data improve upon archival data with the long wavelength baseline. Since the lensed images vary significantly in color and morphology, these new data are useful for a robust identification of the matched counterparts in the lensed images of each source, and in distinguishing the sources from each other.

We follow the naming scheme of Bayliss et al. (2011b) for the giant arcs; however, the exact locations of constraints within each arc are slightly different, owing to the superior *HST* resolution. Source A, at $z_{\text{spec}} = 2.198$, is identified northwest of the cluster core, as a giant arc of three merging images. The

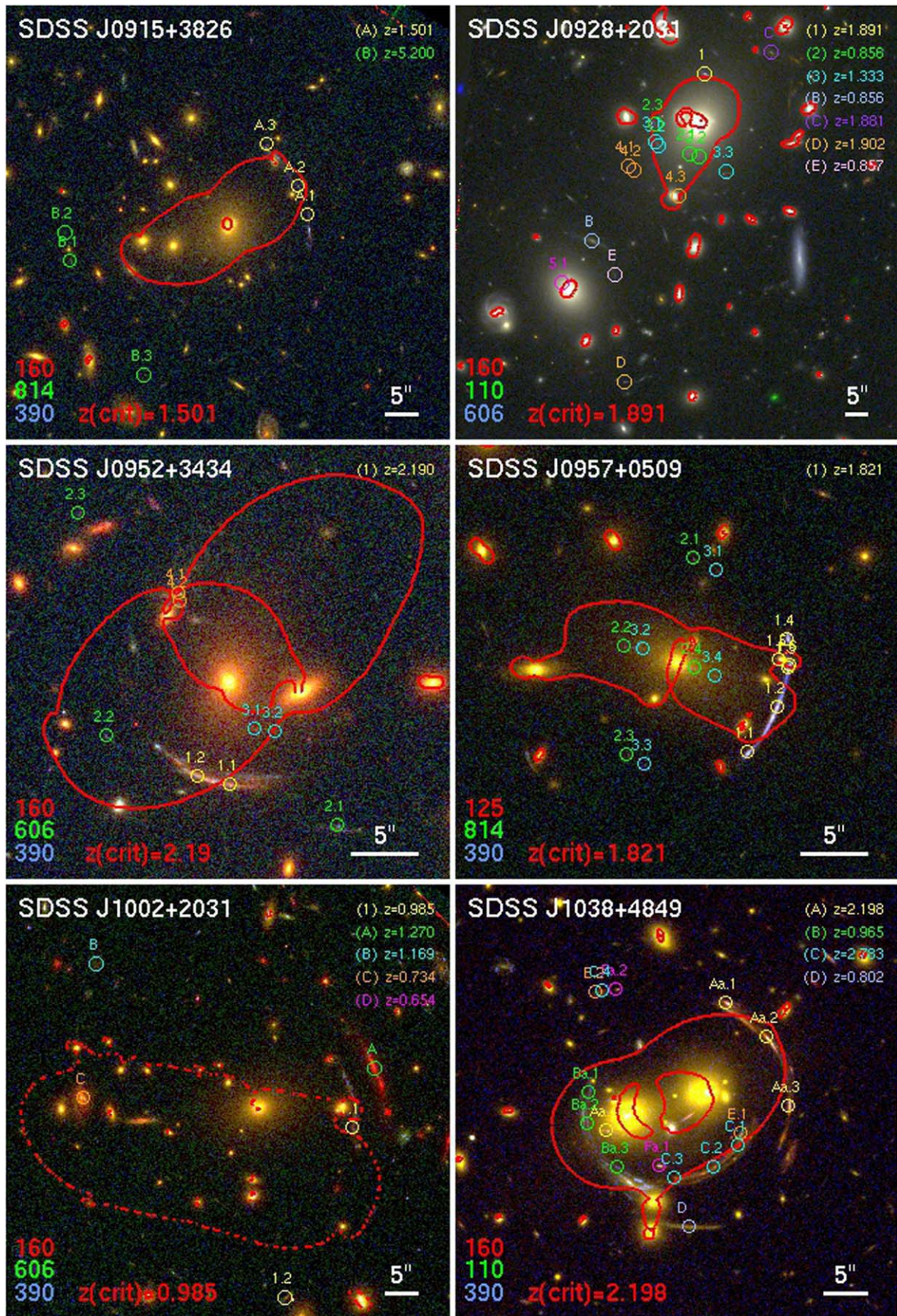


Figure 2. Same as Figure 1, for the clusters SDSS J0915+3826, SDSS J0928+2031, SDSS J0952+3434, SDSS J0957+0509, SDSS J1002+2031, and SDSS J1038+4849. The coordinates, redshifts, and references are tabulated in Table 5.

images are highly magnified in the tangential direction, and several emission clumps can be isolated in each. The source is likely a galaxy pair. We identify a fourth image of this source east of the cluster core.

Source B, at $z_{\text{spec}} = 0.9652$ is seen as a giant arc southeast of the cluster core, brightest in the UVIS bands. The lens model clarifies the lensing configuration of this system: the source galaxy appears to be a spiral galaxy with bright bulge and two loose spiral arms. The central part of the galaxy has one image, that appears slightly distorted in the tangential direction. This is the brightest part of this arc, labeled as image B1 in Bayliss et al. (2011b). In the source plane, some emission knots in one of the spiral arms cross the caustic, forming the elongated giant arc Ba.1, Ba.2, Ba.3.

Source C, at $z_{\text{spec}} = 2.7830$, is lensed into a giant arc composed of three merging images south of the core, and a newly identified counter image north-northeast of the core. The model predicts a demagnified central image for this source, two to four magnitudes fainter, in the light of the central galaxies. We do not identify this image in the current data depth.

Source D in Bayliss et al. (2011b), at $z_{\text{spec}} = 0.802$, is a distorted singly imaged galaxy, and not used as a constraint in the lens model.

We identify two new lensed galaxies. Source E is likely part of system C; however, since it has significantly bluer color than system C we leave its redshift as a free parameter. The model-predicted redshift for this source is consistent with that of source C. We identify two images of source F, south and north of the cluster core. A third image is predicted by the lens model to appear near the center of the cluster, predicted to be two magnitudes fainter. We do not identify this demagnified image.

The model is well constrained and is classified in category A.

4.3.13. SDSS J1050+0017

Our lens model of this cluster was presented in Bayliss et al. (2014b), who measured the physical properties of one of the giant arcs (system C, at $z_{\text{spec}} = 3.625$). We refer the reader to this publication for a full description of the lens model and spectroscopic confirmation of the lensed galaxies. We follow the naming scheme of Bayliss et al. (2014b) in the brief description below; see also Table 6 and Figure 3.

We identify several lensed sources in the field of SDSS J1050+0017. Source A has two images: a giant tangential arc south of the cluster center, and a radial arc north of the BCG. We identify three images of source B, a faint tangential arc and a counter image. Source C has four images, two of them form the giant arc northwest of the cluster center, and the other two appear northeast and south of the BCG. Source D has four images around the cluster core, and we identify two images each for sources E and F. The model only uses as constraints the spectroscopically confirmed systems: A, C, and D. The model is well constrained and is classified in category A.

4.3.14. SDSS J1055+5547

During the UVIS observation of SDSS J1055+5547, the fine guidance sensors failed to lock on one of the two guide stars, and the *HST* visit was executed with only one guide star and gyro control. As a result, the UVIS observation of this cluster failed. The WFC3-IR imaging in F110W and F160W were not significantly affected. Our request for a re-observe of

the failed visits was denied due to STScI's strict policy of not re-observing failed observations when more than 90% of the targets in the program are complete. Since the UVIS data were critical for the science outcome of GO-13003, this cluster was excluded from the analysis of the lensed background sources. Nevertheless, we provide a lens model for this cluster, from a combination of the WFC3-IR data and archival Subaru imaging in *g*, *r*, and *i* (see Oguri et al. 2012 for details of the Subaru observation of this field). Figure 3 is a color rendition made from the F160W and F110W in red and green, respectively, and Subaru *r* band in blue. The *HST* data are superior in resolution, and the Subaru data complement them with a broad wavelength coverage which is useful for a robust identification of lensed features. Furthermore, we identify the cluster-member galaxies in this field from the Subaru data, using the *r* and *i* bands.

The cluster lenses several background galaxies, four of them were identified and targeted for spectroscopy by Bayliss et al. (2011b). The lensed images of source A ($z_{\text{spec}} = 1.250$) and source B ($z_{\text{spec}} = 0.936$) appear in the south of the field. Nearby galaxies complicate the lensing configuration of A and B. Source C ($z_{\text{spec}} = 0.777$) in Bayliss et al. (2011b) is a single image of a background galaxy. Source D was targeted for spectroscopy, but did not yield a redshift measurement. We identify a candidate counter image for this system. We identify other lensing features around the cluster core, as listed in Table 6. The model is well constrained and is classified in category A.

4.3.15. SDSS J1110+6459

The lensing analysis and spectroscopic observations of SDSS J1110+6459 are presented in Johnson et al. (2017b) in more detail. We identify four multiply imaged lensed galaxies, denoted A, B, C, D in Figure 3. The main arc, A, is a giant arc formed by a naked-cusp configuration of three merging images of the same source galaxy. In Johnson et al. (2017b) we measured a source redshift $z_{\text{spec}} = 2.4812$ from Gemini spectroscopy of all three arcs, and identified more than 20 emission knots in each of the three segments of the arc, thanks to the high tangential magnification. In Johnson et al. (2017a, 2017b) and Rigby et al. (2017) we measured their size, luminosity, and star formation rate, and find that the typical source-plane unlensed size is <100 pc. System B is a five-image set, comprised of three tangential and two radial arcs, with distinctive color and morphology. System C is detected with two secure images. A third candidate is predicted by the model but not unambiguously confirmed. System D is identified as three separate emission knots near system A (labeled D, E, F in Johnson et al. 2017b). It is not spectroscopically confirmed; however, as its deflection angle is slightly different than that of system A we conclude that it is a separate galaxy from system A, which happens to be on the same line of sight. The best-fit model redshift for this system is $z_{\text{model}} = 2.37$.

We refer the reader to Johnson et al. (2017b) for the full details of the lens model of SDSS J1110+6459. In short, this cluster was modeled using the hybrid *Lenstool* method, with the cluster potential modeled as a combination of mass components centered on grid nodes, following the prescription of Jullo & Kneib (2009). The halos of cluster galaxies were added as described in Section 4.1. The model is well constrained and is classified in category A.

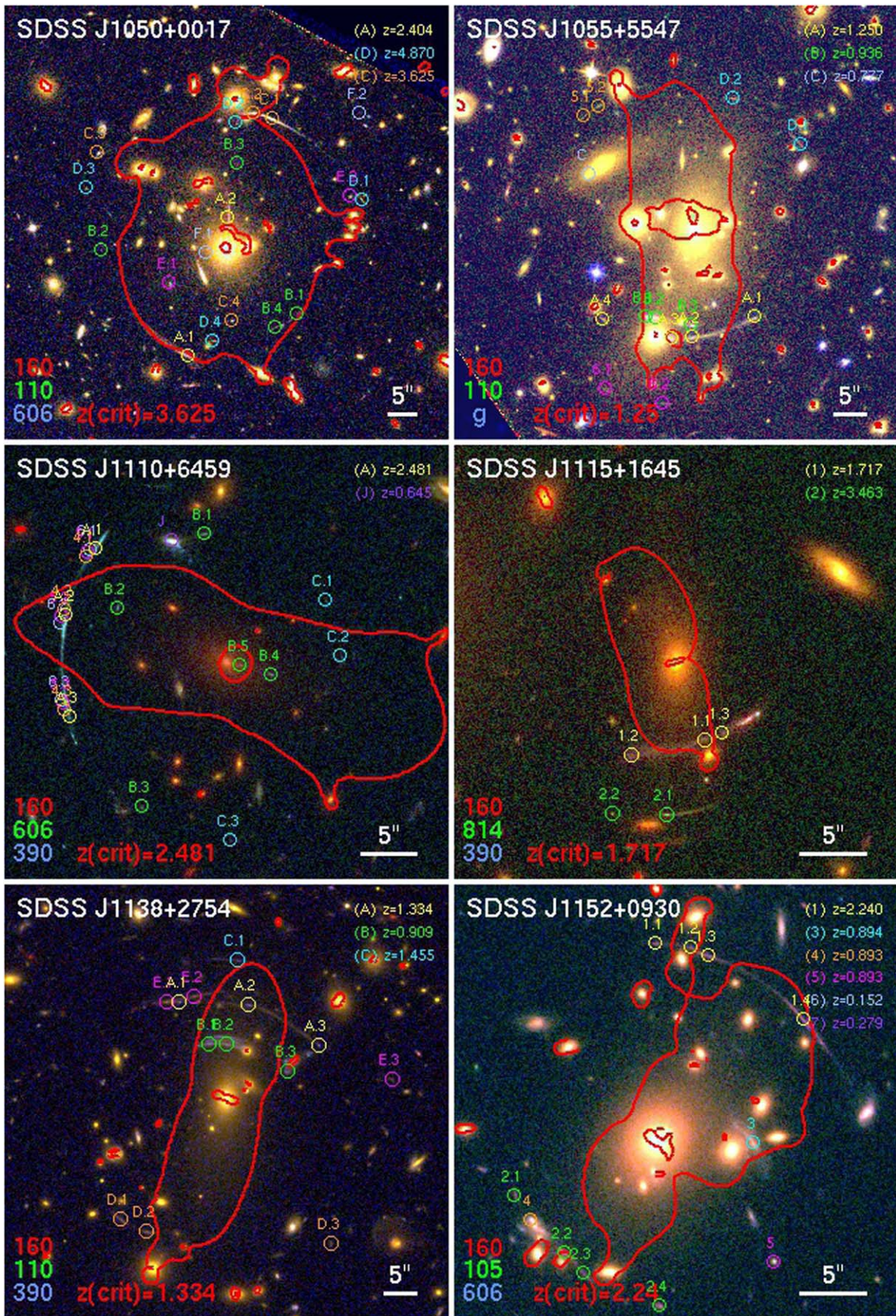


Figure 3. Same as Figure 1, for the clusters SDSS J1050+0017, SDSS J1055+0017, SDSS J1110+6459, SDSS J1115+1645, SDSS J1138+2754, and SDSS J1152+0930. The coordinates, redshifts, and references are tabulated in Table 6.

We also note a “jellyfish” galaxy in this cluster at $z_{\text{spec}} = 0.6447$, spectroscopically confirmed at the cluster redshift near image B.1 (Johnson et al. 2017b). Based on its morphology, this galaxy is likely going through a rapid epoch of star formation as it falls into the cluster (Sun et al. 2010; Ebeling et al. 2014; McPartland et al. 2016).

4.3.16. SDSS J1115+1645

Two lensed galaxies are spectroscopically confirmed in the field of SDSS J1115+1645, both south of the cluster BCG. The redshift of System 1 was measured by Stark et al. (2013), $z_{\text{spec}} = 1.7170$. The redshift of system 2 was measured by Bayliss (2012), $z_{\text{spec}} = 3.4630$. The SDSS DR12 catalog provides spectroscopic redshift of another cluster galaxy at $z_{\text{spec}} = 0.5350$, at a projected radius of $51''.2$ from the BCG.

We identify a foreground structure on the line of sight to the lensing cluster, likely a cluster or a group, at $z_{\text{spec}} \sim 0.19$. The structure appears as a clear red sequence in the color–magnitude diagram of the field. Three galaxies in this cluster/group have spectroscopic redshifts in SDSS DR12, $z_{\text{SDSS}} = 0.19107$, 0.19372 , 0.19602 , within $\sim 3'$ from the lens. The foreground cluster/group is likely boosting the lensing efficiency of SDSS J1115+1645, as seen in other strong-lensing selected clusters (Bayliss et al. 2014a). The lensing evidence suggests that the cluster at $z_{\text{lens, spec}} = 0.537$ is responsible for the observed lensing configuration; however, due to the small number of constraints the current analysis cannot quantify the contribution of the intervening structure. The model is classified in category *B* because, although it has lensing constraints from two galaxies, they are both on the south side of the cluster leaving its north region underconstrained.

4.3.17. SDSS J1138+2754

Five lensed galaxies are identified in this field. All the spectroscopic redshifts were measured by Bayliss et al. (2011b). Source A has three images north of the BCG; all three images were spectroscopically confirmed at $z_{\text{spec}} = 1.334$. Source B, at $z_{\text{spec}} = 0.909$, has three images, two of them form a thick arc north of the BCG. Source C is likely a single image, also north of the BCG, with a tentative redshift $z_{\text{spec}} = 1.455$. Two images of source D were also identified and targeted by Bayliss et al. (2011b) but the spectra did not yield a redshift measurement. We identify a candidate third image for this system. The new *HST* data help discriminate the different part of what looks like a single giant arc in the ground-based data. We identify a new lensed candidate, labeled E.

We measure a photometric redshift for source D, $z_{\text{phot}} = 2.94$ from the *HST* and *Spitzer* photometry. Since the images of this galaxy are the only constraints south of the BCG, we use the photometric redshift as a prior in our analysis. The model is well constrained and is classified as *A*–. A spectroscopic redshift measurement of source D would add confidence to model predictions south of the core.

4.3.18. SDSS J1152+0930

System 1 forms a faint thin giant arc northwest of the BCG, identified as source D in Bayliss et al. (2011b); we rename the lensed features in this field for clarity. The arc is fairly smooth in the *HST* data with no prominent substructure. A faint elongated arc appears in the southwest of the cluster, which we interpret as four images of a lensed galaxy. Other faint arc-like features are

observed in the data; however, we are unable to confirm additional multiple-image lensing constraints. We measure a redshift for system 1 of $z_{\text{spec}} = 2.24$, from tentative [C III] 1907, C III] 1909 Å lines in low signal-to-noise multi-slit spectra using IMACS on the *Magellan* Baade telescope, observed in 2014 April. The same observations result in spectroscopic redshift of two foreground sources at $z_{\text{spec}} = 0.152$ (source 6) and $z_{\text{spec}} = 0.279$ (source 7). We confirm the redshifts of background sources that were formerly measured by Bayliss et al. (2011b) for the galaxies labeled 3 (A2) and 4 (A3); however, the *HST* data, as well as the lens model, indicate that these are single images. Given the similar redshifts of galaxies 3, 4, 5, $z_{\text{spec}} \sim 0.893$, it is likely that they are part of a small background group. The lens model is based on the northwest and southeast arcs, with the redshift of the former used as a fixed constraint. Table 6 lists the positions that were used as constraints. However, due to the relative smooth appearance of the faint arcs, it is difficult to identify the exact locations of the counterparts of each multiply imaged feature. The model is classified as *A*–. A spectroscopic redshift measurement of source #2 would add confidence to the model in the southeast area.

4.3.19. SDSS J1152+3313

Bayliss et al. (2011b) measured the redshifts of two lensed galaxies in this cluster: source A ($z_{\text{spec}} = 2.491$), which forms the giant arc in the west, and two images of source B ($z_{\text{spec}} = 4.1422$). With the *HST* data, the internal structure of the giant arc is resolved, and we identify several unique features in it that are used as lensing constraints. We find that the giant arc is made of three merging images of the background galaxy. In addition, we identify three counter-images, for a total of six detectable images for this system. A seventh image is predicted by the lens model near the center of the southern central galaxy (near A.6); several features are detected in the galaxy light, but as they cannot be uniquely matched with features in the other arcs, we do not use this image as a constraint. For source B we identify four images, with a fifth, demagnified image predicted by the lens model to appear near the center of the south central galaxy, but is too faint to be uniquely identified in the galaxy light. We identify two images of a new lensed galaxy, labeled C, with two images, and a demagnified third predicted near the core of the north central galaxy. It was not targeted for spectroscopy and therefore its redshift is unknown. The model is well constrained and is classified in category *A*.

4.3.20. SDSS J1156+1911

In the field of SDSS J1156+1911 we detect one giant arc at $z_{\text{spec}} = 1.543$ (Stark et al. 2013). We assume a cluster redshift from the spectroscopic measurement of its BCG, $z_{\text{BCG, spec}} = 0.54547 \pm 0.00013$ from SDSS. The BCG redshift was also measured by Stark et al. (2013). We do not detect a counter image for the giant arc. The lens model and the color gradients within the arc indicate that the east and west portions of the arc are not multiply imaged. The source galaxy crosses two caustics in the source plane, resulting in magnification and stretching of only a small part of the galaxy. The model is reliable for reconstructing the morphology of the lensed galaxy, and can explain its lensing geometry. Given the limited lensing constraints we classify it in category *B*.

4.3.21. SDSS J1207+5254

SDSS J1207+5254, at $z = 0.275$, was reported by Kubo et al. (2010). The cluster core contains several elliptical galaxies, and not one dominant central galaxy. The small curvature of the $z_{\text{spec}} = 1.926$ giant arc is a result of an elongated projected mass density distribution, caused by a secondary halo, which coincides with the bright elliptical galaxy to the northeast. The cluster was observed in our Gemini program, but the pipeline failed to generate useable flat fields for most of the mask due to scattered light from the bright acquisition stars.

Interestingly, an overdensity of luminous red galaxies is apparent in the WFC/IR data northwest of the cluster center, and based on the color and brightness it is likely a background structure.

The giant arc in SDSS J1207+5254 is a naked-cusp configuration of three images, two of which are partial images. We identify 10 individual emission knots that are used as constraints; no counter image is identified in the data beyond the giant arc, as expected in such configuration. A secondary system of two high-confidence arcs is identified southwest of the cluster center, with unknown redshift. A third image in this system is predicted by the lens model to be embedded in the light of a cluster-member galaxy, and is visually confirmed; this third image is not used as a constraint in the model. The lens model is classified as $B+$, with higher uncertainties in the southwest region.

Comparing the new *HST* data and *gri* Gemini/GMOS observations taken on 2008 December 23 as part of GN-2008A-Q-25, we found in the GMOS data a point-like source that does not have a counterpart in the *HST* image, at R.A., decl. = [181.8982, 52.918553]. Since this source only appears in the archival images we were unable to confirm it spectroscopically. If extragalactic, this source could be a supernova (SN) at the cluster redshift without an apparent host, i.e., an intracluster SN. These have been shown to compose as much as 20% of cluster SNe (Gal-Yam et al. 2003; Sharon et al. 2010; Sand et al. 2011). Alternatively, the transient could be a supernova in the foreground or behind the cluster, with an undetected faint host. The magnification at the position of the transient depends on the source redshift, but given its close proximity to the cluster center (see Figure 4) it could be significant, ranging from 1.8 for a source at $z = 0.4$, to 7 for a source at $z = 1$, and ~ 17 for a source at $z = 2$. The transient appears in two of the three bands, with $g > 25.9 \pm 0.3$, $r = 23.87 \pm 0.07$, and $i = 23.28 \pm 0.08$. The duration of the GMOS observations was 10 minutes, during which the position of the source remains stable. For a thorough discussion of SN alternatives in a single-epoch discovery we refer the reader to Gal-Yam et al. (2002) and Sharon et al. (2010).

4.3.22. SDSS J1209+2640

The discovery of the lensing cluster SDSS J1209+2640 was reported by Ofek et al. (2008). This paper identified several lensed candidates, and measured the redshift of the brightest arc, A, $z_{\text{spec}} = 1.018$. Bayliss et al. (2011b) measured spectroscopic redshifts of source B, $z_{\text{spec}} = 0.789$, and C, $z_{\text{spec}} = 3.948$. With archival WFC2 data and the broad wavelength coverage made available by our new *HST* data, we identify the counter-images of C, and several new arcs. We keep the ID names of systems A, B, and C, and relabel the new systems below.

Source 4.1 is approximately the suggested candidate D in Ofek et al. (2008). Bayliss et al. (2011b) obtained a spectrum of this arc, but was unable to secure spectroscopic redshift for it. We identify a candidate counter image for it in the south part of the field, which was labeled H2 in Ofek et al. (2008).

Source 5 is identified as a radial pair southwest of the BCG, 5.1 and 5.2, with a counter image in the north part of the field. This system has unique colors and diffuse surface brightness that helps in its identification.

Source 6, with six images, is bright in the WFC3-IR bands and virtually absent from the optical data. Since we also detect this source in our *Spitzer* imaging, we conclude that it is likely a $z \sim 1$ –3 dusty galaxy, which is supported by the lens model. A cluster galaxy in the north part of the cluster core complicates the lensing configuration and is responsible for three of the images.

We identify two candidate images for source 7, one of which is the arc labeled I in Ofek et al. (2008).

The lensing signal of this cluster is modeled with one halo for the cluster and halos for the cluster galaxies. We let the parameters of the galaxy near the three north images of system 6 to be solved for by the lens model. We note that to reproduce the lensing evidence this model requires external shear in addition to these components. The model is well constrained, and classified in category A.

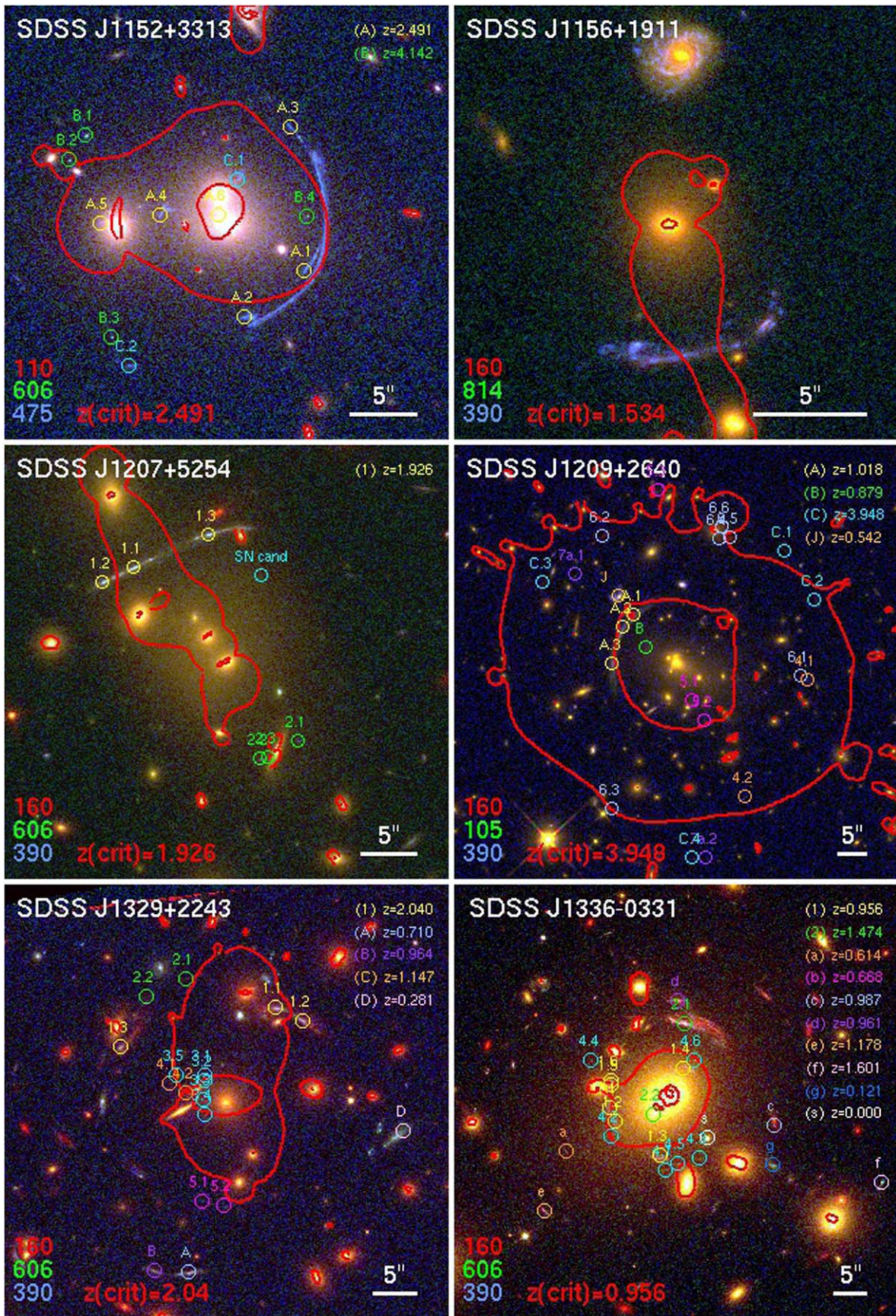
Our Gemini/GMOS spectroscopy did not yield new redshifts for arc candidates in this field. We add 10 spectroscopic redshifts for cluster-member galaxies to the measurements of Bayliss et al. (2011b) and update the velocity dispersion of this cluster (Table 2). Finally, we note a galaxy that is likely undergoing ram pressure stripping, near the core of the cluster, at R.A., decl. = [182.3517695, 26.68261135], labeled J. Its redshift as well as that of a nearby galaxy were measured by Ofek et al. (2008) as $z_{\text{spec}} = 0.542$.

4.3.23. SDSS J1329+2243

The main lensed system in this field has three images of a galaxy at $z_{\text{spec}} = 2.04$, north of the cluster center. Spectroscopic confirmation of the three images was obtained with Gemini/GMOS-North (Bayliss et al. 2014a). From the same multi-slit observations, we measure the spectroscopic redshifts of other sources in the field.

The orientation of sources A and B, located south of the BCG, suggest that they may be multiple images of the same source. We rule out this scenario based on their different spectroscopic redshifts, $z_{\text{spec}} = 0.710$ and $z_{\text{spec}} = 0.964$, respectively, which also places them outside of the strong-lensing region. Similarly, the spectroscopic redshifts of galaxies C and D confirm that they are single images.

We identify a few faint sources as multiple-image candidates based on colors and morphology, as listed in Table 7 and plotted in Figure 4. We used all the knots in system 1 as constraints in the model, the two secure images of system 2, and the two secure radial images of system 4, the latter two systems with unknown redshift set as a free parameter. The lensing morphology of system 3 is complicated by several cluster galaxies in the core of the cluster. The five listed images have similar colors and surface brightnesses in all the bands in which they appear; however, we cannot definitively determine whether they are all images of the same source. The lens model is consistent with several images being produced at this region. Nevertheless, these images are not used as constraints in the



model published here. Deeper imaging to secure the identification of system 3, and spectroscopic redshifts of sources 2, 4, 5 would strengthen the model and increase its fidelity. It is otherwise well constrained, and we classify it as A–.

4.3.24. SDSS J1336–0331

We identify two giant arcs in this field. Southeast of the BCG, we detect an elongated arc (source 1), with a counter image on the opposite side of the BCG. The giant arc is composed of at least two images, with a cluster-member galaxy adding complexity to the lensing potential that results in partial arcs between this galaxy and the BCG. A bright lensed galaxy (source 2) appears north of the BCG, with a significantly redder core. We identify and spectroscopically confirm a radial arc south of the BCG, making this a system of two images. Two other faint galaxies are identified as multiply imaged lensed systems and used as constraints. We observed SDSS J1336–0331 with the *Magellan* Clay 6.5 telescope using the LDSS3 instrument. Long-slit spectroscopy of the two bright components of source 1 south of the BCG confirm their spectroscopic redshift at $z_{\text{spec}} = 0.96$. IMACS multi-slit mask spectroscopy observed with the *Magellan* 6.5 m Baade telescope confirms the radial arc south of the BCG (labeled 2.2 in Figure 4) as a counter image of 2.1, the giant arc to the north, at $z_{\text{spec}} = 1.47$. The same spectrum reveals multiple emission lines from the cluster redshift, likely from the galaxies at the core of the cluster. This spectrum, as well as a prominent dust lane in the light of the BCG, indicates significant star formation at the core of this cluster. The model is well constrained, and classified in category A.

4.3.25. SDSS J1343+4155

A giant arc appears at the east side of the cluster core, with $z_{\text{spec}} = 2.091$ (Diehl et al. 2009). The *HST* resolution reveals some substructure in the giant arc, which helps with its interpretation as three merging partial images of the background galaxy, which crosses a naked caustic cusp in the source plane. There are no counter-images identified, as expected in this configuration. The discovery and spectroscopy of a $z_{\text{spec}} = 4.994$ lensed $\text{Ly}\alpha$ emitting galaxy in the field of SDSS J1343+4155 was reported by Bayliss et al. (2010). A candidate counter image that was suggested by Bayliss et al. (2010) appears to not have the exact same color and morphology as the spectroscopically confirmed image. We therefore do not use it as a lensing constraint. The model does not predict multiple images for the $\text{Ly}\alpha$ emitter. We identify three faint images of a candidate third lensed galaxy. The improvement upon the model presented in Bayliss et al. (2010) includes revised constraints: we use the identified emission knots in the giant arc, remove the candidate counter image of the $\text{Ly}\alpha$ emitter, and add candidate 2 with free redshift. In addition, we account for contributions from individual cluster galaxies, which was not implemented in Bayliss et al. (2010). Since all the lensing constraints appear in one side of the cluster core, degeneracies between model parameters increase the uncertainties, especially in regions which have no lensing constraints (i.e., the southwest part of the cluster, where the $\text{Ly}\alpha$ source appears). We therefore classify it in category B.

4.3.26. SDSS J1420+3955

The appearance of two giant arcs in ground-based optical data led to the selection of this cluster as a strong lens. The *HST* imaging reveal several other lensed galaxies, resulting in a total of 10 lensed systems in this field. The lensing evidence indicates that SDSS J1420+3955 is a complex structure. Bayliss et al. (2011b) report the spectroscopic redshifts of two giant arcs, labeled A and B. The lensing configuration of arc A, at $z_{\text{spec}} = 2.161$, appears to be affected by a cluster galaxy, forming at least five images or partial images of the source around the cluster member, with a sixth complete image $25''7$ north of it. The unique colors and morphology make this a confident identification. Arc B is at $z_{\text{spec}} = 3.066$; the *HST* imaging reveals multiple emission knots and enables the identification of a counter image, B.3.3.

Newly identified lensed features include a red giant arc (source 3) with a counter image, bright in the WFC3/IR imaging, as well as other lensed galaxies, some of which form radial arcs. We identify two radial images of source 4. A group of three sources 5, 6, and 7, have four identified images each. Source 8 forms three images near one of the cluster galaxies near the core, and a fourth image northwest of the core of the cluster. None of these newly identified sources have spectroscopic redshifts measured.

We also identify strong-lensing evidence around two bright cluster galaxies located $53''$ and $68''$ west of the BCG. We use these lensing features to constrain the contribution from these structures to the overall lensing mass of SDSS J1420+3955.

Overall, the cluster is constrained by images from 10 lensed galaxies, providing ample positional constraints. However, the lack of spectroscopic redshifts for all but two galaxies is a limitation. A spectroscopic redshift of any of sources 5, 6, 7, or 8 would place the cluster in category A; we currently classify it as A–.

4.3.27. SDSS J1439+1208

The main arc in this field appears as a merging pair (source 1), with redshift $z_{\text{spec}} = 1.494$, measured from *Magellan*/FIRE spectroscopy. A preliminary lens model predicts the location and morphology of a counter image (1.3) and radial arc, readily discovered in the *HST* imaging (1.4), with robust confirmation by colors and morphology. We further discover another set of two images (2.1, 2.2) and a candidate radial image (2.4). The lens model predicts a fourth image between images 2.1 and 2.2. We detect a likely candidate counter image in that location (2.3).

We pursued spectroscopic confirmation of the lensed candidates, using the *Magellan* Baade 6.5 m telescope with the IMACS camera. On 2013 March 17 we obtained long-slit spectra of B1, 1.2, and 2.2. On 2014 April 26 we obtained multi-slit spectroscopy, targeting the candidate counter image of the main arc, 1.3, arc 2.1, and the candidate arc B2. These observations resulted in spectroscopic redshift of 2.1, $z_{\text{spec}} = 1.580$ from [O II] 3727, 3729 Å line. The slit on 1.3 was unfortunately placed on a chip gap, and did not yield data. A comparison between the spectra of B1 and B2 leads to the conclusion that they are not images of the same source. We observe a strong emission line in the spectrum of B1 that is not observed in B2, placing it at $z_{\text{spec}} = 3.48$ if it is coming from $\text{Ly}\alpha$. A low-confidence emission line in the MOS spectrum of B1 suggests that it may be at $z_{\text{spec}} = 1.53$, if this line is [O II] 3727, 3729 Å.

The model is well constrained and classified in category A.

4.3.28. SDSS J1456+5702

The *HST* imaging of SDSS J1456+5702 reveals the details of an extended, low-surface brightness arc. While giant arcs are often observed to be long and thin, this one has an unusual width of $3''.4$. A counter image is detected close to the BCG. Due to its low surface brightness, this was the only main arc in GO-13003 that lacked spectroscopic redshift prior to its *HST* observation. We secured a spectroscopic redshift for the giant arc, $z_{\text{spec}} = 2.366$, from S II, O I, Si II, and C II lines in a Blue Channel spectrum obtained at MMT on 2014 May 4 (PI: Bayliss).

The lensing morphology of this system is primarily of three images: the giant arc in the south, a counter image north of the BCG, and a demagnified image near the core. The morphology of the giant arc is slightly complicated by cluster-member galaxies, causing some parts of the central region of the giant arc to be highly magnified and with added multiplicity.

Bayliss et al. (2011b) measured spectroscopic redshifts of three other galaxies in this field (Table 8), most notably two galaxies at similar redshift, A1 and A2, on opposite sides of the cluster core. The *HST* imaging indicates that these galaxies are not images of the same source; the lens model is also consistent with these galaxies being single images. The model is well constrained and classified in category A.

4.3.29. SDSS J1522+2535

In this field, we find one highly magnified galaxy, with five multiple images. The galaxy is clearly resolved, and displays a bright core (brighter in the infrared bands) as well as spiral structure. The proximity to cluster galaxies complicates the lensing configuration. In particular, a cluster galaxy is superimposed near the core of image 1.1 but does not significantly distort it. Images 1.4 and 1.5 are more strongly affected by the BCG and other bright galaxies near it. Nevertheless, due to its unique colors and morphology, all five images of the lensed galaxy are robustly identified. Moreover, all the images are spectroscopically confirmed by our Gemini/GMOS spectroscopy (Table 11), at $z_{\text{spec}} = 1.7096$. Some of the lens model parameters of the three galaxies in close proximity to the lensed images were left as free parameters. The model is well constrained and classified in category A.

4.3.30. SDSS J1527+0652

SDSS J1527+0652 was reported in Koester et al. (2010), as a highly magnified galaxy at $z_{\text{spec}} = 2.76$. The bottom-right panel in Figure 5 zooms in on the arc, which appears $14''.5$ south of the core of a galaxy cluster that is outside of the figure. The foreground cluster does not have one obvious central galaxy. The added resolution of the *HST* observations reveal that the lensing geometry is locally dominated by the lensing potential of an elliptical galaxy, boosted by the cluster potential. The arc is composed of three partial images; counter-images are neither detected nor predicted by the lens model. The arc at $z_{\text{spec}} = 2.76$ is the most obvious lensing feature in this field; however, it is not sufficient for constraining the mass distribution of the cluster itself. To constrain the cluster halo, we rely on several faint multiply imaged lensed galaxies. These galaxies are not spectroscopically confirmed. The lens model is consistent with the velocity dispersion measured from spectroscopy of 14 cluster

galaxies (Bayliss et al. 2011a), $\sigma_v = 923 \pm 233 \text{ km s}^{-1}$. The conversion between velocity dispersion and the PIEMD σ_v parameter is given in Elíasdóttir et al. (2007).

R. Bordoloi et al. (2020, in preparation) observed this galaxy with the Keck Cosmic Web Imager (KCWI) on UT 2017 June 21, with a field of view of $16''.5 \times 20''.4$, resulting in IFU spectroscopy of the main highly magnified galaxy and nearby galaxies. The observations indicate that some of the emission that is evident in our *HST* imaging comes from a line-of-sight interloper at $z_{\text{spec}} = 2.543$. *Magellan*/MagE observations (Rigby et al. 2018b) reveal several intervening absorption systems (J. Rigby et al. 2020, in preparation), including one at $z_{\text{spec}} = 2.543$, for which an emission-line component is seen in the KCWI data, which explains diffuse emission seen in the *HST* imaging. J. Rigby et al. (2020, in preparation) also find several other intervening absorption systems at lower redshifts. The KCWI data also measure the redshift of several nearby galaxies, finding a small group at $z \simeq 0.43$, including the galaxy nearest to the main arc. We therefore employ an iterative approach in modeling the lens. We first compute a lens model for the cluster as explained above; we then treat the cluster as providing cosmic shear, and proceed to model the galaxy near the main arc. The large number of observed emission clumps constrain the lens model, which is composed of the lens galaxy as well as contribution from external shear.

We also note a fainter arc at R.A., decl. = [231.92365, 6.862152778] caused by lensing by an elliptical galaxy close to the edge of our *HST* field of view. This lensed arc was not used to constrain the lens model.

The lensing constraints available are not sufficient for a robust model of the galaxy cluster; we classify the cluster model in category C. Nevertheless, like other models with similar lensing configuration (e.g., SDSS J1004–0103), this model provides a reliable description of the lensing configuration of the main arc in the field. For its high magnification uncertainty, we classify the lens model that is used for this lensed source in category B.

4.3.31. SDSS J1531+3414

We refer the reader to Sharon et al. (2015) for detailed description of the lensing analysis of SDSS J1531+3414. We provide a short description here. In the field of this cluster we confirm three strongly lensed galaxies. Source 1 with five images, source 2 with five images, and source 3 with a tangential and radial arc. Bayliss et al. (2011b) observed this field with multi-object spectroscopy, and secured a redshift for source 1 at $z_{\text{spec}} = 1.096$. For the other two sources, only lower limits were measured, $z > 1.49$ for both. Our lensing analysis in Sharon et al. (2015) confirms that galaxies A5, A6, B2, and C1 in Bayliss et al. (2011b) are single images. The model is well constrained and classified in category A.

4.3.32. SDSS J1604+2244

This cluster was identified as a strong lens based on a bright elongated arc, labeled A, at $z_{\text{spec}} = 1.184$, which is located $\sim 18''$ west of the two bright galaxies that dominate the cluster center. We measured the redshift of this arc, as well as six cluster-member galaxies, using Gemini GMOS (program GN11AQ19). The cluster is at relatively low redshift compared to other clusters in this sample, $z_{\text{cluster}} = 0.286$. The arc appears to be a single image. Although other arc-like features are

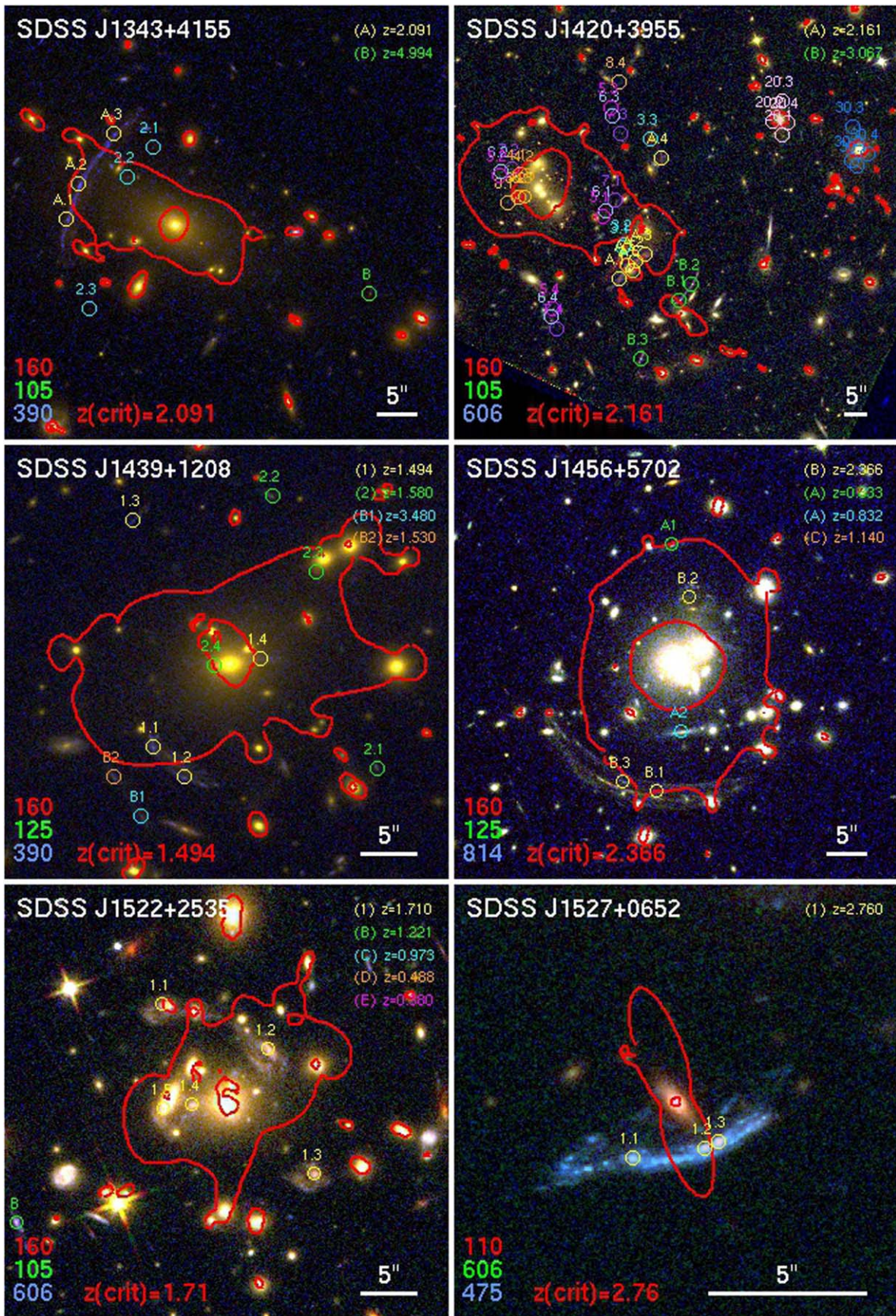


Figure 5. Same as Figure 1, for the clusters SDSS J1343+4155, SDSS J1420+3955, SDSS J1439+1208, SDSS J1456+5702, SDSS J1522+2535, and SDSS J1527+0652. The coordinates, redshifts, and references are tabulated in Table 8.

observed in the *HST* data, we are able to identify only one secure family of multiple images that can be used to constrain the lens model. The system, labeled as source 1, consists of five images with distinct morphology and color. We measure the photometric redshift of the three images that are not too blended in the light of the foreground galaxies, finding $z_{\text{phot}} = 0.53$. We compute a lens model with the photometric redshift used as prior, $0.5 < z_1 < 0.8$. We require that the lens model does not produce counter-images for singly imaged galaxies. The model is classified in category *B*; a spectroscopic redshift of source 1 would improve its reliability.

4.3.33. SDSS J1621+0607

Three arcs were identified by Bayliss et al. (2011b), who were able to measure spectroscopic redshifts for two of them. Source A, which has two images, is a Ly α emitter at $z_{\text{spec}} = 4.131$. Source B is at $z_{\text{spec}} = 1.1778$. Source C was targeted for spectroscopy, but the observation did not yield a redshift. With the *HST* data, we find that A.1 is buried in the light of a foreground galaxy; we do not identify a third image for this source. We find two counter-images for arc B, and obtained spectroscopic confirmation with *Magellan* using the LDSS3 long-slit on 2013 May 2. From the lensing analysis, we conclude that the arc identified as B1 by Bayliss et al. (2011b) is a merging pair of two partial images, whereas the other two images are complete. We relabel B1 as 2.1 and 2.2, and the complete images are 2.3 and 2.4. The region of highest surface brightness in 2.3 and 2.4 falls outside of the caustic, and thus is not seen in the merging pair 2.1–2.2. We use three distinct features in this galaxy as constraints—the bright core of the galaxy in 2.3 and 2.4, a dark dust lane, and a blue region that appears clearly in all the images. There is no robust identification of a counter image for C; we therefore do not use it as a constraint in the lens model. Its elongation and curvature suggest that it is lensed. From the best-fit model, this arc could be a merging pair straddling the critical curve at $z \sim 2.4$, with a counter image near R.A., decl. = [245.3811204, 6.123205304]. We identify a few plausible candidate images within 2'' of this location. This interpretation is consistent with the conclusion of Bayliss et al. (2011b), that arc C is likely in the “redshift desert,” based on the lack of emission lines in its Gemini/GMOS spectrum. The lens model is consistent with the velocity dispersion that we measure from our IMACS MOS observation (Table 2), supplemented with the redshifts reported by Bayliss et al. (2011b). The model is well constrained and classified in category *A*.

4.3.34. SDSS J1632+3500

This field displays two giant arcs, approximately 15'' east and west of the cluster core. Spectroscopic redshifts were obtained from Gemini North GMOS observations in 2012 April 15 for the two sources: source 1 at $z_{\text{spec}} = 1.235$, and source 2 at $z_{\text{spec}} = 2.265$. The spectrum of the bright region in the eastern giant arc indicates the possible presence of an AGN, inferred from He I emission. The same Gemini observations secure spectroscopic redshift of a star-forming galaxy that is likely a cluster member, projected to be near the cluster core, with somewhat large velocity offset from the mean ($z_{\text{spec}} = 0.454$ and $z_{\text{spec}} = 0.466$, respectively), but within 2.5σ of the projected velocity dispersion. Other background, foreground, and cluster members with spectroscopic redshift measurement are listed in

Tables 9 and 11. Our *HST* imaging data confirm that the two giant arcs are extremely distorted lensed images; however, no counter-images are identified. We used the extended shape of the giant arcs as constraints in the lens model. In both cases, the brightest part of the galaxy (i.e., the galaxy core) lies outside of the lensing caustic and thus are singly imaged. Two other possible lensed systems are identified and their positions are used as constraints in the lens model; their redshifts are left as free parameters. The mass model is well constrained by the two giant arcs. However, the lensing magnification of the giant arcs has high uncertainty due to its close proximity to the critical curve, where small variations in the model result in large change in magnification. We therefore classify the model in the *B* category. Spectroscopic confirmation of the two lensed candidates is likely to improve the model.

4.3.35. SDSS J1723+3411

The bright arc in this field is one of the brightest lensed galaxies known to date, at $z_{\text{spec}} = 1.3294 \pm 0.0002$ Kubo et al. (2010). The source is lensed into five images, two of which merge to form the bright arc, images 1.1 and 1.2. The third and fourth images, 1.3 and 1.4, are easily identified, and the fifth is a demagnified image near the core of the BCG, 1.5. Since the BCG light drops out from our bluest *HST* filter, the fifth image is clearly identified 0.3'' from the center of the galaxy. We identify four images of a likely galaxy pair, labeled as sources 2 and 3. A redshift for source 2 was measured from *HST* grism data (GO-14230, PI: Rigby), $z_{\text{spec}} = 2.165$ based on [O III] 4959, 5007 Å emission lines. We were unable to derive a redshift for source 3. The lens model published here assumes that source 3 is at the same redshift as source 2; we have computed models that leave this redshift as a free parameter, and these models are indistinguishable from the one with a fixed redshift for source 3. A distorted red galaxy east of the images 2.2 and 3.2 is likely a single image. The model is well constrained and labeled as *A*.

Interestingly, the *HST* data reveal a dust lane in the light of the BCG, indicating possible recent star formation (e.g., Cooke et al. 2016).

4.3.36. SDSS J2111–0114

Carrasco et al. (2017) obtained spectroscopy of 46 cluster members in this field from the Very Large Telescope. In calculating the cluster redshift and velocity dispersion (Table 2), we add to these measurements six additional redshifts for cluster members from Bayliss et al. (2011b). The spectroscopic redshift of the main arc, $z_{\text{spec}} = 2.858$, is adopted from Bayliss et al. (2011b). The strong-lensing constraints in this field are the main arc and two other candidate systems, all of which are in naked-cusp configuration. Since all the lensing constraints appear south of the BCG, this field is underconstrained on the north side. We therefore classify this model in category *B*. The lens model is in good agreement with the observed velocity dispersion.

4.3.37. SDSS J2243–0935

The primary arc in this field is an elongated arc at $z_{\text{spec}} = 2.09$ (Bayliss et al. 2011b). Rigby et al. (2018b) report that the lensed source hosts a broad-line AGN, based on broad rest-frame UV emission lines. This interpretation is confirmed by the morphology of this galaxy in the *HST* imaging, which shows a point-source embedded in a spatially extended host (labeled 1.1 in Figure 7). This straight arc is located 52'' east of

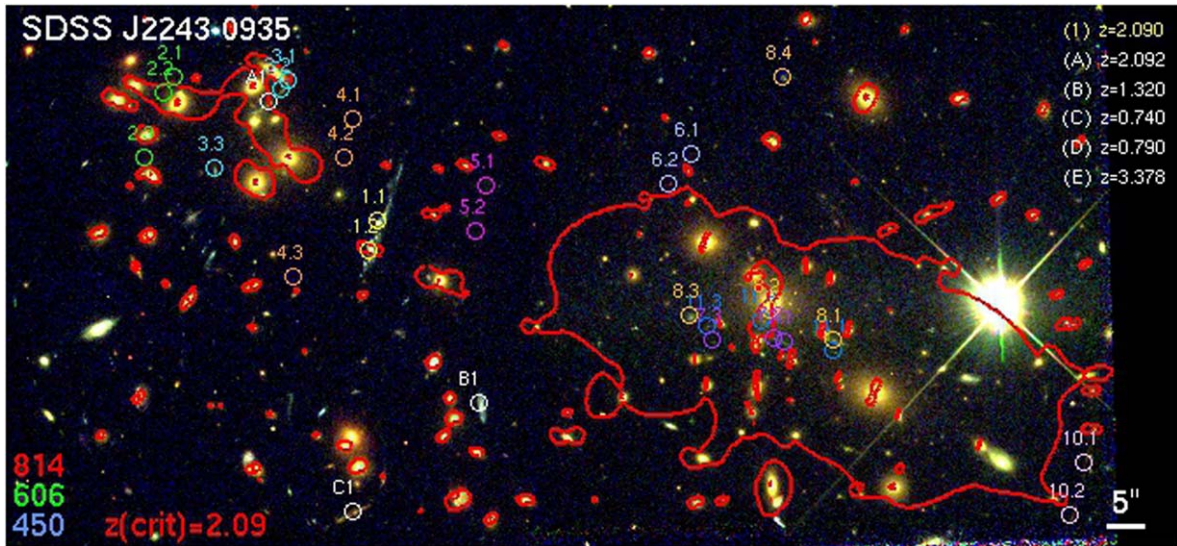


Figure 7. Same as Figure 1, for the cluster SDSS J2243–0935. The coordinates, redshifts, and references are tabulated in Table 10.

the core of the cluster, in the direction to a prominent group of cluster-member galaxies. This lensing morphology, showing an arc with minimal or no curvature, is typically found in cluster mergers or bimodal distribution when arcs form in the region between two dominant halos. We find that the morphology of this arc is also affected by a small cluster-member galaxy projected on the line of sight, resulting in multiple images of a few of the emission knots in the host galaxy.

The F390W imaging data reveal a faint point-source embedded in the light of the cluster galaxy, separated from its core, likely a counter image of the AGN nucleus (labeled 1.2). One of the MagE slits in the observations of Rigby et al. (2018b) partially covers this source. A careful extraction and inspection of the two-dimensional spectrum at the position of the candidate counter image suggest faint emission from this region; however, the signal-to-noise ratio is not sufficient to spectroscopically confirm it as a counter image of the nucleus. The AGN (1.1) clearly appears as an X-ray point source in archival *Chandra* observations of this field, detected at 7.5σ above the background. The X-ray emission from the positions of the optical point source (1.2) is detected at 2.2σ above the background, confirming that it is likely a counter image of the AGN.

We identify several other multiply imaged lensed galaxies around the west (main) and east (secondary) halos of this cluster core that help constrain the lens model. However, spectroscopic observations with the IMACS instrument on the *Magellan* Baade telescope, targeting the lensed images, did not yield redshifts for these multiple-image families. Source 3 appears close to a source that was observed by Bayliss et al. (2011b) to be at $z_{\text{spec}} = 2.092$; however, the color and morphology of this source are not consistent with the sources identified as multiply imaged, and we therefore conservatively leave the redshift of source 3 as a free parameter. Several instances of galaxy–galaxy lensing are identified within the *HST* field of view, owing to the overall high projected mass density in this region of the sky. We note these identifications, as well as the lensing constraints, in Table 10.

The lack of spectroscopic redshifts of multiply imaged lensed galaxies leave this cluster underconstrained. The redshifts of all

but source 1 are left as free parameters. However, to improve the accuracy of the lens model and avoid catastrophic solutions we place priors on the redshift parameter of the most prominent arcs in each subhalo, informed by their photometric redshifts. These are source #2 near the east halo, with photometric redshifts measured from images 2.1 and 2.3, and source #8 near the west halo, with photometric redshifts measured from images 8.1 and 8.3. We use the photometric redshift posterior distribution to inform our redshift priors, $2.90 < z_2 < 3.10$ and $2.95 < z_8 < 3.05$.

This cluster was independently identified via its X-ray signal by Ebeling et al. (2010) and is also known as MACS J2243–09. Schirmer et al. (2011) use weak lensing to map the cosmic web around this cluster and report on the filamentary structure around it. They report a mass of $M_{200} = 1.31^{+0.25}_{-0.20} \times 10^{15} h_{70}^{-1} M_{\odot}$ within $r_{200} = 2.13^{+0.18}_{-0.12} h_{70}^{-1}$ Mpc. Our strong-lensing analysis estimates that the mass within 500 kpc is $M \sim 7.5 \times 10^{14} M_{\odot}$. Although highly uncertain due to the lack of spectroscopic redshifts, this mass estimate is consistent with the weak lensing measurement. We classify this model as A–. Its fidelity can be improved by securing spectroscopic redshifts of some of the lensed galaxies.

5. Discussion

In this paper, we assign a subjective qualitative assessment to each model, based on the availability and distribution of constraints, availability of spectroscopic redshifts, and ability of the lens model to consistently reproduce the lensing constraints. As we note in Section 4.3, the literature often quantifies the relative quality of lens models by quoting the rms of the scatter between the observed and model-predicted image-plane locations of lensed images (image plane rms, or rmsi). However, while the rmsi provides a useful comparative goodness-of-fit when assessing different models that use the same constraints, it may be misleading, especially in under-constrained systems. A comparison between the quality categories and the best-fit model rmsi is shown in Figure 8. As expected, the rmsi is not a good predictor of the subjective quality categories. Models in category A span a large range of image plane rms, between $0''.1$ and $0''.65$. On the other hand, some of the poor models with few constraints appear to have

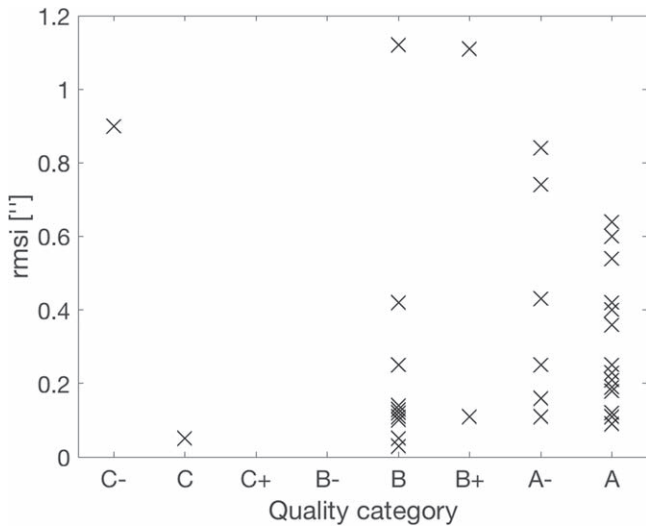


Figure 8. Comparison of image plane rms (rmsi) and the qualitative model quality assessment. We find that the rmsi is not a good indicator of model quality.

very small rmsi ($\text{rmsi} < 0''.2$), which does not encompass the systematic sources of model error. Johnson & Sharon (2016) explore this behavior using simulated data and show that the rmsi is not a predictor of model quality when considering models with different numbers of constraints: while the accuracy and precision of magnification and mass improves with larger number of constraints, the rmsi becomes worse; this is due to the finite flexibility of most lens-modeling algorithms. We therefore encourage the user to consider the noted strengths and shortcomings of each model, given in Section 4.3, when using the lens model outputs.

We estimate the effective Einstein radius of each cluster, $\theta_E = \sqrt{A/\pi}$, the radius of a circle with the same area A enclosed by the tangential critical curve for a source at redshift $z_s = 2$, and tabulate them in Table 2. The effective Einstein radius correlates with the area in which strong lensing can occur around each lens, and depends primarily on the mass enclosed in the core of the cluster. From the lens models presented in this work, we find that the SGAS-*HST* clusters span a large range of effective Einstein radii, $1''.3 < \theta_E < 23''.1$, with a median $\theta_E = 10''.8$. Notably, θ_E does not correlate with the total mass of the cluster (estimated from their velocity dispersion as M_{200}), as can be seen in Figure 9. A more comprehensive analysis of indicators of lensing strength, extending beyond this strong-lensing sample, will be presented in a future paper (C. Fox et al. 2020, in preparation). Since strong-lensing measures the projected mass density at the core of the cluster, combining strong lensing with a mass estimate at the outskirts can put constraints on the slope of the mass profile and can measure its concentration (e.g., Gralla et al. 2011; Oguri et al. 2012; Merten et al. 2015). An investigation of the concentration–mass relation in a large sample of strong-lensing clusters is underway (J. Remolina González et al. 2020, in preparation).

6. Summary

We present strong lens models for 37 galaxy clusters from the SGAS Large *HST* program, GO-13003. The lens models are constrained by positions of multiply imaged lensed galaxies that

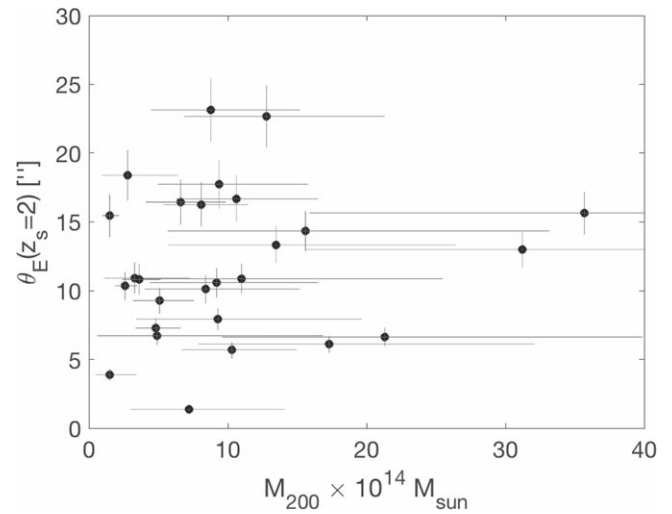


Figure 9. Comparison the effective Einstein radii and the dynamical mass M_{200} (Table 2) shows no correlation between the two; see Section 5. The uncertainties on the Einstein radii are estimated at 10%.

were uniquely identified in the *HST* imaging. We measured spectroscopic redshifts for lensed galaxies from data obtained with *Magellan*, *Gemini*, *APO*, and *HST*. The lensing constraints that were used in this work, including image positions and redshifts from this work and from the literature, are listed in the Appendix.

Magnification from strong-lensing clusters of galaxies enables studies of the magnified sources behind them. The magnification boost increases the observed brightness of the background galaxies, leading to higher signal-to-noise ratio per unit time of spectroscopic observations, allowing us to study galaxies that would otherwise require an unrealistic amount of observing time with current facilities. The lensing distortion increases the observed spatial resolution of the background source, which enables studies of star formation on spatial scales as small as a few tens of parsecs at cosmic noon.

In order to take full advantage of the lensing magnification in analyzing the background galaxies, one needs to incorporate the information from lens models. Once the properties of the foreground lens are properly modeled, the derived lens model outputs are used in order to convert the observed measurements of background sources to their intrinsic ones. The deflection maps are used to ray-trace the light from the image plane to the source plane, and thus reconstruct the undistorted image of the source galaxy. They are used to determine the morphology of the source and measure or constrain the spatial extent of substructure within the source. The magnification, which may vary significantly along giant arc-like images in the image plane, linearly converts between lensed and unlensed luminosity, and properties that are derived from it (i.e., star formation rate, stellar mass).

With this publication, we release the lens model outputs of each field. The availability of constraints in each field varies, and depends not only on the lensing strength of the foreground cluster, but also on the extent of follow-up observations, depth of the available data, spatial distribution of constraints, and in many cases, fortuitous alignment between the sources and the lens. A description of the models and an assessment of their

reliability are given in this paper. The lensing outputs are specific to the redshifts in the system, but can be converted to any source redshift; the equations needed for this conversion can be found in Johnson et al. (2014, Section 4.3). We also provide a set of model outputs computed from the MCMC process, from which uncertainties can be estimated. The public models were generated and tested for compatibility with *Lenstool* version 7.1. The high-level data products and reduced *HST* imaging data are hosted on the Multimission Archive at the Space Telescope Science Institute (MAST),¹⁸ and can be accessed via doi:[10.17909/t9-cqjt-y020](https://doi.org/10.17909/t9-cqjt-y020).

Support for *HST* program GO-13003 was provided by NASA through a grant from the Space Telescope Science Institute, which is operated by the Association of Universities for Research in Astronomy, Inc., under NASA contract NAS 5-26555. Based on observations made with the NASA/ESA *Hubble Space Telescope*, obtained at the Space Telescope Science Institute, which is operated by the Association of Universities for Research in Astronomy, Inc., under NASA contract NAS 5-26555. These observations are associated with programs GO-13003, GO-14622, GO-14230, GO-14896. Some of the data presented in this paper were obtained from the Multimission Archive at the Space Telescope Science Institute (MAST). These data are associated with programs GO-11974, GO-11100. K.S. acknowledges support from the University of Michigan’s President’s Postdoctoral Fellowship. K.E.W. gratefully acknowledge support by NASA through Hubble Fellowship grant #HF2-51368 awarded by the Space Telescope Science Institute, which is operated by the Association of Universities for Research in Astronomy, Inc., for NASA.

M.B.B. acknowledge support by NASA through grant HST-GO-14896-01. H.D. acknowledges support from the Research Council of Norway. Based on observations obtained at the Gemini Observatory, which is operated by the Association of Universities for Research in Astronomy, Inc., under a cooperative agreement with the NSF on behalf of the Gemini partnership: the National Science Foundation (United States), the National Research Council (Canada), CONICYT (Chile), the Australian Research Council (Australia), Ministério da Ciência, Tecnologia e Inovação (Brazil) and Ministerio de Ciencia, Tecnología e Innovación Productiva (Argentina). This paper includes data gathered with the 6.5 m *Magellan* Telescopes located at Las Campanas Observatory, Chile. Observations reported here were obtained at the MMT Observatory, a joint facility of the University of Arizona and the Smithsonian Institution. This work makes use of the Matlab Astronomy Package (Ofek 2014). We thank the anonymous referee for their thoughtful review of this manuscript

Appendix A Lensing Constraints

This appendix tabulates the identified multiply imaged lensed sources in each field. For each source, we list the coordinates of the observed images and of emission knots within these image that were used as lensing constraints. Where available, we list the spectroscopic or photometric redshift of the background source. The coordinates and redshifts of other foreground or background sources are given as well.

Tables 4–10 correspond to Figures 1–7. (Tables 4, 5, 6, 7, 8, 9, and 10 correspond to Figures 1, 2, 3, 4, 5, 6, and 7, respectively.)

¹⁸ <https://archive.stsci.edu/hlsp/sgas/>

Table 4
List of Lensing Constraints for Clusters Shown in Figure 1

ID	R.A. J2000	Decl. J2000	z_{spec}	z_{spec} Reference	Notes
SDSS J0004−0103					
1.1	1.215462	−1.055917	1.681	Rigby+18	
1.2	1.215350	−1.055859			
1.3	1.214755	−1.055367			
1a.1	1.215583	−1.055996			
1a.2	1.215140	−1.055762			
1a.3	1.214867	−1.055521			
1b.1	1.215821	−1.055905			
1b.2	1.215276	−1.055667			
1b.3	1.214801	−1.055190			
1 c.1	1.214795	−1.055314			
1 c.2	1.215224	−1.055719			
1 c.3	1.215689	−1.055942			
1d.1	1.215385	−1.055875			
1d.2	1.215428	−1.055900			
SDSS J0108+0624					
1.1	17.174978	6.412078	1.91	Rigby+18	
1.2	17.176051	6.412092			
1a.1	17.175900	6.412684			
1a.2	17.175025	6.412060			
1b.1	17.175964	6.412493			
1b.2	17.174992	6.412063			
1 c.1	17.174932	6.412091			
1 c.2	17.176030	6.411886			
SDSS J0146−0929					
1.1	26.736156	−9.496396	1.9436	This work, FIRE; Stark+13	
1.2	26.730240	−9.495975			
1.3	26.730774	−9.495248			
1.4	26.733138	−9.501209			
1.5	26.730610	−9.499755			
11.1	26.736201	−9.496491			
11.2	26.730257	−9.495890			
11.3	26.730918	−9.495014			
12.1	26.736238	−9.496558			
12.2	26.730315	−9.495800			
12.3	26.730955	−9.494963			
12.4	26.733018	−9.501201			
13.1	26.736386	−9.496849			
13.2	26.730378	−9.495644			
13.3	26.731003	−9.494875			
14.1	26.736177	−9.496564			
14.2	26.730148	−9.496054			
2.1	26.733406	−9.495280	2.3660	This work, IMACS	
2.2	26.734766	−9.502288			
2.3	26.733561	−9.497364			Candidate
21.1	26.733440	−9.495278			
21.2	26.734715	−9.502318			
E	26.73471004	−9.502603976	0.7962	This work, IMACS	Single image, near 2.2
D	26.72841422	−9.493789352	2.6623	This work, IMACS	Single image
G	26.72786667	−9.498882957	0.4485	This work, IMACS	Single image
SDSS J0150+2725					
1.1	27.505066	27.426420	1.0800	This work, APO	2012 Jan 20
1.2	27.504752	27.426018			
1.3	27.503328	27.425350			
1.5	27.503476	27.426849			
11.1	27.505501	27.427167			
11.2	27.503379	27.426822			

Table 4
(Continued)

ID	R.A. J2000	Decl. J2000	z_{spec}	z_{spec} Reference	Notes
2.1	27.509517	27.426914	...		
2.2	27.508971	27.425031			
SDSS J0333–0651					
1.1	53.271663	–6.856274	1.5700	This work, FIRE	Possibly single image
1.2	53.270623	–6.854172			
2.1	53.268675	–6.862509	...		Galaxy–galaxy lensing
2.2	53.268182	–6.862460			
3.1	53.267530	–6.854139	...		Candidate
3.2	53.269571	–6.854654			Candidate
4.1	53.265041	–6.856527	...		Candidate
4.2	53.265125	–6.857559			Candidate
4.3	53.266938	–6.859791			Candidate
SDSS J0851+3331					
B.1	132.908460	33.517522	1.3454	Bayliss+11	
B.2	132.908210	33.518601			
B.3	132.914270	33.523888			
B.4	132.912760	33.517752			Candidate radial arc
B1.1	132.908500	33.517410			
B1.2	132.908200	33.518789			
D.1	132.909040	33.521854	1.79	GO-14622, PI: Whitaker	
D.2	132.908460	33.515032			
D.3	132.914680	33.517739			
D.4	132.914390	33.523319			
D.5	132.912310	33.518961			
D1.1	132.909056	33.521854			
D1.2	132.908477	33.515017			
D1.3	132.914686	33.517705			
D1.4	132.914439	33.523272			
D1.5	132.912316	33.519003			
E.1	132.915050	33.512978	1.88	GO14622, PI: Whitaker	
E.2	132.915260	33.513197			
E.3	132.916770	33.513843			
E.4	132.915660	33.512927			
E.5	132.916314	33.513417			Candidate partial image
E1.1	132.915090	33.513014			
E1.2	132.915220	33.513155			
E1.3	132.916820	33.513869			
A	132.904550	33.520420	1.6926	Bayliss+11	Single image
C	132.917233	33.522550	1.2539	Bayliss+11	Single image

Note. Lensing constraints and other background or foreground galaxies with spectroscopic redshifts in the fields of SGAS-*HST* clusters SDSS J0004–0103, SDSS J0108+0624, SDSS J0146–0929, SDSS J0150+2725, SDSS J0333–0651, and SDSS J0851+3331. The IDs of images of lensed galaxies are labeled as *AB.X* where *A* is a number or a letter indicating the source ID (or system name); *B* is a number or a letter indicating the ID of the emission knot within the system; and *X* is a number indicating the ID of the lensed image within the multiple-image family.

References. Rigby et al. (2018b), Stark et al. (2013), Bayliss (2012), Bayliss et al. (2010, 2011b, 2014b), Kubo et al. (2010), Johnson et al. (2017b), Ofek et al. (2008), Diehl et al. (2009).

(This table is available in machine-readable form.)

Table 5
List of Lensing Constraints for Clusters Shown in Figure 2

ID	R.A. J2000	Decl. J2000	z_{spec}	z_{spec} Reference	Notes	
SDSS J0915+3826						
A.1	138.908560	38.450062	1.5010	Bayliss+10,11		
A.2	138.909080	38.451231				
A.3	138.910690	38.452942				
Aa.1	138.910780	38.452817				
Ab.2	138.908530	38.449497				
Ab.3	138.910140	38.452420				
Ac.1	138.908590	38.448827				
Ac.2	138.910780	38.452575				
Ac.3	138.909643	38.451724				
B.1	138.920960	38.448191	5.2000	Bayliss+10,11		
B.2	138.921280	38.449322				
B.3	138.917120	38.443534				
SDSS J0928+2031						
1	142.018470	20.532302	1.8910	This work, FIRE		
2.1	142.019460	20.527312	0.8555	This work, GMOS		
2.2	142.018810	20.527153				
2.3	142.021730	20.529145				
3.1	142.021720	20.528090	1.3327	This work, GMOS		
3.2	142.021500	20.527861				
3.3	142.017040	20.526253				
4.1	142.023490	20.526590	...		Candidate	
4.2	142.023160	20.526368				
4.3	142.020190	20.524736				
5.1	142.027803	20.519392	...		Candidate radial arc near south halo	
B	142.025835	20.522019	0.8563	This work, GMOS	Single distorted image near south core	
C	142.014117	20.533593	1.8806	This work, FIRE	Single image	
D	142.023744	20.513353	1.9020	This work, FIRE	Single image	
E	142.024390	20.519945	0.8565	This work, GMOS	Single image	
SDSS J0952+3434						
1.1	148.167560	34.577362	2.1900	Kubo+10		
1.2	148.168350	34.577527				
2.1	148.164870	34.576523	...			
2.2	148.170630	34.578348				
2.3	148.171320	34.582908				
3.1	148.166930	34.578496	...			
3.2	148.166430	34.578438				
4.1	148.168820	34.581285	...			
4.2	148.168810	34.581105				
SDSS J0957+0509						
1.1	149.411832	5.156988	1.8210	Bayliss+11		
1.2	149.411235	5.157918				
1.3	149.410998	5.158717				
1.4	149.411013	5.159312				
1.5	149.411191	5.158897				
1.6	149.410982	5.158763				
2.1	149.412957	5.160956	...			
2.2	149.414378	5.159153				
2.3	149.414307	5.156947				
2.4	149.412930	5.158728				

Table 5
(Continued)

ID	R.A. J2000	Decl. J2000	z_{spec}	z_{spec} Reference	Notes
3.1	149.412476	5.160714	...		
3.2	149.413997	5.159112			
3.3	149.413951	5.156746			
3.4	149.412504	5.158557			
SDSS J1002+2031					
1.1	150.607950	20.516451	0.985	This work, GMOS	Giant arc
1.2	150.610894	20.509550	...		Candidate counter image
A	150.607010	20.518948	1.270	This work, GMOS	Single image
B	150.619170	20.523185	1.169	This work, GMOS	Single image
C	150.619715	20.517718	0.734	This work, GMOS	Single image
D	150.596254	20.514684	0.654	This work, GMOS	Single image
SDSS J1038+4849					
Aa.1	159.676917	48.825040	2.198	Bayliss+11	A in Bayliss+11
Aa.2	159.675061	48.823981			
Aa.3	159.674008	48.821871			
Aa.4	159.682485	48.821117			
Ab.1	159.676659	48.824781			
Ab.2	159.676111	48.824502			
Ab.3	159.674327	48.820902			
Ab.4	159.682786	48.821117			
Ba.1	159.683319	48.822281	0.9652	Bayliss+11	B in Bayliss+11
Ba.2	159.683427	48.821341			
Ba.3	159.682014	48.820000			
Bb.1	159.683632	48.821441			
Bb.2	159.683631	48.821830			
Bb.3	159.682515	48.820109			
C.1	159.676358	48.820663	2.7830	Bayliss+11	C in Bayliss+11
C.2	159.677509	48.819994			
C.3	159.679320	48.819666			
C.4	159.682720	48.825398			
Ca.1	159.676575	48.820271			
Ca.2	159.675840	48.820938			
Ca.4	159.682460	48.825365			
Cb.1	159.676223	48.820798			
Cb.2	159.678027	48.819816			
Cb.3	159.679071	48.819662			
E.1	159.676264	48.821019	...		
E.2	159.683006	48.825364			
Fa.1	159.680013	48.820036	...		
Fa.2	159.682045	48.825450			
Fb.1	159.680118	48.820050	...		
Fb.2	159.681968	48.825473			
D	159.678666	48.818142	0.8020	Bayliss+11	Single image

Note. Lensing constraints and other background or foreground galaxies with spectroscopic redshifts in the fields of SGAS-*HST* clusters SDSS J0915+3826, SDSS J0928+2031, SDSS J0952+3434, SDSS J0957+0509, SDSS J1002+2031, and SDSS J1038+4849. The IDs of images of lensed galaxies are labeled as *AB.X* where *A* is a number or a letter indicating the source ID (or system name); *B* is a number or a letter indicating the ID of the emission knot within the system; and *X* is a number indicating the ID of the lensed image within the multiple-image family.

References. Rigby et al. (2018b), Stark et al. (2013), Bayliss (2012), Bayliss et al. (2010, 2011b, 2014b), Kubo et al. (2010), Johnson et al. (2017b), Ofek et al. (2008), Diehl et al. (2009).

(This table is available in machine-readable form.)

Table 6
List of Lensing Constraints for Clusters Shown in Figure 3

ID	R.A. J2000	Decl. J2000	z_{spec}	z_{spec} Reference	Notes
SDSS J1050+0017					
A.1	162.668160	0.280149	2.4040	Bayliss+14	
A.2	162.666250	0.286671			
B.1	162.663000	0.282145	...		
B.2	162.672260	0.285115			
B.3	162.665830	0.289216			
B.4	162.664060	0.281483			
D.1	162.659930	0.287493	4.8700	Bayliss+14	
D.2	162.665880	0.291141			
D.3	162.672950	0.288075			
D.4	162.666960	0.280862			
C.1	162.664160	0.291329	3.6250	Bayliss+14	
C.2	162.665070	0.291628			
C.3	162.672400	0.289762			
C.4	162.666086	0.281812			
E.1	162.669020	0.283582	...		
E.2	162.660530	0.287685			
F.1	162.667300	0.285000	...		
F.2	162.660050	0.291583			
SDSS J1055+5547					
A.1	163.764788	55.802890	1.2500	Bayliss+11	
A.2	163.769380	55.802066			
A.3	163.770840	55.802015			
A.4	163.775825	55.802779			
B.1	163.772724	55.802923	0.9360	Bayliss+11	
B.2	163.771971	55.802880			
B.3	163.769481	55.802571			
Ba.1	163.772510	55.802923			
Ba.2	163.772229	55.802893			
Ba.3	163.769323	55.802577			
D.1	163.761436	55.809967	...		D in Bayliss+11
D.2	163.766349	55.811872			
5.1	163.777241	55.811158	...		
5.2	163.776207	55.811533			
6.1	163.775678	55.799939			
6.2	163.771550	55.799350			
C	163.776906	55.808742	0.777	Bayliss+11	Single image
SDSS J1110+6459					
A.1	167.581480	64.999411	2.4812	Johnson+17, Stark+13	
A.2	167.583170	64.997795			
A.3	167.582980	64.995273			
B.1	167.575130	64.999798	...		
B.2	167.580210	64.997948			
B.3	167.578800	64.993072			
B.4	167.571270	64.996332			
B.5	167.573070	64.996565			
C.1	167.568090	64.998147	...		
C.2	167.567230	64.996781			
C.3	167.573630	64.992252			Candidate
4.1	167.582030	64.999212	...		
4.2	167.583280	64.997903			
4.3	167.583280	64.995456			

Table 6
(Continued)

ID	R.A. J2000	Decl. J2000	z_{spec}	z_{spec} Reference	Notes
5.1	167.581910	64.999308	...		
5.2	167.583400	64.997748			
5.3	167.583360	64.995603			
6.1	167.581760	64.999396	...		
6.2	167.583470	64.997575			
6.3	167.583400	64.995701			
J	167.577020	64.999612	0.6447 2	Johnson+17	“Jellyfish” galaxy
SDSS J1115+1645					
1.1	168.767840	16.758996	1.7170	Stark+13	
1.2	168.769390	16.758679			
1.3	168.767450	16.759129			
2.1	168.768650	16.757464	3.4630	Bayliss+12	
2.2	168.769810	16.757478			
SDSS J1138+2754					
A.1	174.539460	27.912498	1.3340	Bayliss+11	
A.2	174.536280	27.912373			
A.3	174.533020	27.910710			
B.1	174.538084	27.910779	0.9090		
B.2	174.537286	27.910748			
B.3	174.534447	27.909638			
C.1	174.536764	27.914191	1.4550	Bayliss+11	Single image
D.1	174.542160	27.903572	...	This work	$z_{\text{phot}} = 3.2$
D.2	174.540960	27.903079			
D.3	174.532440	27.902590			
E.1	174.540057	27.912498	...		
E.2	174.538768	27.912722			
E.3	174.529624	27.909298			Candidate
SDSS J1152+0930					
1.1	178.197480	9.508144	2.2400	This work, IMACS	D1,D2 in Bayliss+11
1.2	178.196754	9.508056			
1.3	178.196378	9.507894			
1.4	178.194424	9.506574			
2.1	178.200403	9.502987	...		C1 in Bayliss+11
2.2	178.199381	9.501804			
2.3	178.198991	9.501391			
2.4	178.197409	9.500721			
3	178.195447	9.504058	0.8945	This work, IMACS; Bayliss+11	Single image; A2 in Bayliss+11
4	178.200080	9.502489	0.893	This work, IMACS; Bayliss+11	Single image; A3 in Bayliss+11
5	178.195037	9.501626	0.893	Bayliss+11	Single image; A1 in Bayliss+11
6	178.195959	9.498743	0.1520	This work, IMACS	Foreground
7	178.196645	9.498887	0.2790	This work, IMACS	Foreground

Note. Lensing constraints and other background or foreground galaxies with spectroscopic redshifts in the fields of SGAS-*HST* clusters SDSS J1050+0017, SDSS J1055+0017, SDSS J1110+6459, SDSS J1115+1645, SDSS J1138+2754, and SDSS J1152+0930. The IDs of images of lensed galaxies are labeled as $AB.X$ where A is a number or a letter indicating the source ID (or system name); B is a number or a letter indicating the ID of the emission knot within the system; and X is a number indicating the ID of the lensed image within the multiple-image family.

References. Rigby et al. (2018b), Stark et al. (2013), Bayliss (2012), Bayliss et al. (2010, 2011b, 2014b), Kubo et al. (2010), Johnson et al. (2017b), Ofek et al. (2008), Diehl et al. (2009).

(This table is available in machine-readable form.)

Table 7
List of Lensing Constraints for Clusters Shown in Figure 4

ID	R.A. J2000	Decl. J2000	z_{spec}	z_{spec} Reference	Notes
SDSS J1152+3313					
A.1	177.998849	33.227292	2.4910	Bayliss+11	
A.2	178.000309	33.226344			
A.3	177.999189	33.230220			
A.4	178.002384	33.228415			
A.5	178.003857	33.228260			
A.6	178.000963	33.228431			
A1.1	177.998621	33.227558			
A1.2	178.000112	33.226334			
A1.3	177.998987	33.230023			
A1.4	178.002341	33.228479			
A1.5	178.003788	33.228307			
A2.1	177.998551	33.227699			
A2.2	178.000171	33.226303			
A2.3	177.998930	33.229947			
A3.2	178.000151	33.226193			
A3.3	177.998534	33.229282			
A3.4	178.002320	33.228598			
A3.6	178.001038	33.228632			
A4.2	177.999190	33.226691			
A4.3	177.998617	33.229571			
A4.4	178.002181	33.228533			
A4.5	178.003671	33.228277			
A4.6	178.001066	33.228574			
B.1	178.004190	33.230054	4.1422	Bayliss+11	
B.2	178.004590	33.229554			
B.3	178.003560	33.225932			
B.4	177.998780	33.228408			
C.1	178.000480	33.229159	...		
C.2	178.003140	33.225349			
SDSS J1156+1911					
1	179.022440	19.185323	1.5430	Stark+13	
SDSS J1207+5254					
1.1	181.903370	52.918765	1.9260	Kubo+10	
1.2	181.904630	52.918406			
1.3	181.900360	52.919571			
1a.1	181.904920	52.918342			
1a.2	181.902730	52.918963			
1a.3	181.900840	52.919494			
1b.1	181.903940	52.918579			
1b.2	181.904210	52.918498			
1 c.1	181.902350	52.918905			
1 c.2	181.901000	52.919288			
2.1	181.896690	52.914499	...		
2.2	181.898240	52.914044			
2.3	181.897894	52.914102			Candidate
SN cand	181.8982	52.918553			Location of SN candidate, discovered in archival GMOS imaging
SDSS J1209+2640					
A.1	182.350930	26.681689	1.0180	Ofek+08	
A.2	182.351500	26.681164			
A.3	182.352090	26.679416			
B	182.35032	26.680163	0.879	Bayliss+11	
C.1	182.342960	26.684707	3.9480	Bayliss+11	
C.2	182.341400	26.682441			

Table 7
(Continued)

ID	R.A. J2000	Decl. J2000	z_{spec}	z_{spec} Reference	Notes
C.3	182.355790	26.683225			
C.4	182.347856	26.670245			
4.1	182.341782	26.678621	...		
4.2	182.345070	26.673153			Candidate
5.1	182.347890	26.677651	...		
5.2	182.347220	26.676739			
5.3	182.349667	26.687590			
6.1	182.342125	26.678861	...		IR (dusty)
6.2	182.352617	26.685458			
6.3	182.352073	26.672528			
6.4	182.346474	26.685323			
6.5	182.345869	26.685350			
6.6	182.346284	26.685887			
7a.1	182.354066	26.683616	...		
7a.2	182.347138	26.670215			Candidate
7b.1	182.353591	26.684219			
7b.2	182.347467	26.670170			Candidate
J	182.351763	26.682600	0.542	Ofek+08	“Jellyfish” galaxy
SDSS J1329+2243					
1.1	202.392260	22.723947	2.0400	Bayliss+14	Knots in source 1
1.2	202.391340	22.723539			
1.3	202.397396	22.722757			
1b.1	202.391650	22.723738			
1b.2	202.391889	22.723873			
1b.3	202.397483	22.722747			
1 c.1	202.391092	22.723370			
1 c.2	202.392442	22.723829			
1 c.3	202.397387	22.722657			
1d.1	202.390930	22.723279			
1d.2	202.392627	22.723718			
1d.3	202.397329	22.722648			
1e.2	202.392077	22.723914			
1e.1	202.391450	22.723595			
1e.3	202.397453	22.722719			
2.1	202.395249	22.724825	...		Tangential arc, candidate
2.2	202.396536	22.724304			
3.1	202.394619	22.721897	...		Candidate system near radial critical curve
3.2	202.394611	22.721712			
3.3	202.394645	22.721121			
3.4	202.394589	22.720651			
3.5	202.395540	22.721882			
4.1	202.395765	22.721646	...		Candidate
4.2	202.395232	22.721315			
5.1	202.394698	22.718009	...		Tangential arc, candidate
5.2	202.393956	22.717865			
A	202.395142	22.715818	0.7096	This work, GMOS	Single image
B	202.396303	22.715868	0.9644	This work, GMOS	Single image
C	202.396603	22.710030	1.1472	This work, GMOS	Single image
D	202.388014	22.720156	0.2811	This work, GMOS	Single image
SDSS J1336–0331					
1.1	204.002570	−3.525374	0.9556	This work, LDSS3	
1.2	204.002340	−3.525918			

Table 7
(Continued)

ID	R.A. J2000	Decl. J2000	z_{spec}	z_{spec} Reference	Notes
1.3	204.000510	−3.527313			
1.4	203.999560	−3.523771			
1.5	204.002510	−3.524433			
1.6	204.002520	−3.524291			
2.1	203.999500	−3.521916	1.4737	This work, IMACS	
2.2	204.000790	−3.525640		This work, IMACS	Spectroscopically confirmed radial arc
4.1	204.000320	−3.527927	...		
4.2	204.002540	−3.526535			
4.3	203.998900	−3.527469			
4.4	204.003330	−3.523445			
4.5	203.999790	−3.527670			
4.6	203.999120	−3.523427			
a	204.004370	−3.527186	0.6139	This work, IMACS	Possible redshift
b	203.988837	−3.528258	0.6685	This work, IMACS	Single image
c	203.995852	−3.526103	0.9865	This work, IMACS	Single image
d	203.999791	−3.520988	0.9613	This work, IMACS	Single image
e	204.005241	−3.529637	1.1783	This work, IMACS	Single image
f	203.991477	−3.528430	1.6015	This work, IMACS	Single image
g	203.995908	−3.527730	0.1206	This work, IMACS	Foreground
s	203.998599	−3.526622	0.00	This work, IMACS	Star

Note. Lensing constraints and other background or foreground galaxies with spectroscopic redshifts in the fields of SGAS-*HST* clusters SDSS J1152+3313, SDSS J1156+1911, SDSS J1207+5254, SDSS J1209+2640, SDSS J1329+2243, and SDSS J1336−0331. The IDs of images of lensed galaxies are labeled as *AB.X* where *A* is a number or a letter indicating the source ID (or system name); *B* is a number or a letter indicating the ID of the emission knot within the system; and *X* is a number indicating the ID of the lensed image within the multiple-image family.

References. Rigby et al. (2018b), Stark et al. (2013), Bayliss (2012), Bayliss et al. (2010, 2011b, 2014b), Kubo et al. (2010), Johnson et al. (2017b), Ofek et al. (2008), Diehl et al. (2009).

(This table is available in machine-readable form.)

Table 8
List of Lensing Constraints for Clusters Shown in Figure 5

ID	R.A. J2000	Decl. J2000	z_{spec}	z_{spec} Reference	Notes
SDSS J1343+4155					
A.1	205.891790	41.917796	2.0910	Bayliss+11, Diehl+09	
A.2	205.891220	41.919003			
A.3	205.889630	41.920730			
Aa.1	205.889900	41.920332			
Aa.2	205.890240	41.920017			
Aa.3	205.891980	41.916926			
B	205.877930	41.915293	4.994	Bayliss+11	
2.1	205.887850	41.920262	...		
2.2	205.889010	41.919262			
2.3	205.890780	41.914773			
SDSS J1420+3955					
A.1	215.161652	39.914131	2.1610	Bayliss+11	
A.2	215.160340	39.915191			
A.3	215.159600	39.915621			
A.4	215.158280	39.921504			
A.5	215.160952	39.914990			
A.6	215.160582	39.914590			
B.1	215.156830	39.912824	3.0665	Bayliss+11	
B.2	215.155840	39.913817			
B.3	215.159930	39.909231			

Table 8
(Continued)

ID	R.A. J2000	Decl. J2000	z_{spec}	z_{spec} Reference	Notes
Bb.1	215.155430	39.914457			
Bb.2	215.157200	39.912639			
Bb.3	215.159780	39.909520			
3.1	215.161360	39.916025	...		
3.2	215.161250	39.916211			
3.3	215.159150	39.922727			
4.1	215.169607	39.920562	...		
4.2	215.169066	39.920456			
4b.1	215.169749	39.920578			
4b.2	215.168985	39.920438			
5.1	215.162934	39.917972	...		
5.2	215.171229	39.920415			
5.3	215.162289	39.924584			
5.4	215.166954	39.912265			Candidate
6.1	215.162750	39.918301	...		
6.2	215.171055	39.920716			
6.3	215.162135	39.924116			
6.4	215.167052	39.911817			Candidate
7.1	215.161918	39.918919	...		
7.3	215.161482	39.923071			
7.2	215.170257	39.920849			Candidate
7.4	215.166625	39.911040			Candidate
8.1	215.170597	39.918805	...		
8.2	215.169685	39.919134			
8.3	215.169165	39.919150			
8.4	215.161679	39.926218			
20.1	215.148556	39.922919	...		Near NW halo1
20.2	215.149334	39.923745			
20.3	215.148650	39.925028			
20.4	215.148153	39.923660			
30.1	215.142593	39.921047	...		Near NW halo2
30.2	215.143058	39.921337			
30.3	215.142942	39.923436			
30.4	215.141806	39.921806			
SDSS J1439+1208					
1.1	219.792668	12.138371	1.4940	This work, FIRE	2013 Mar 01
1.2	219.791888	12.137640			
1.3	219.793188	12.143946			
1.4	219.789968	12.140544			
1a.1	219.792718	12.138600			
1a.2	219.791448	12.137471			
1a.3	219.793018	12.144041			
1a.4	219.789758	12.140576			
1b.1	219.792568	12.138661			
1b.2	219.791118	12.137460			
1b.3	219.792838	12.144199			
1b.4	219.789508	12.140580			
1 c.1	219.791888	12.137807			
1 c.2	219.792268	12.138138			
2.1	219.787058	12.137849	1.5800	This work, IMACS	
2.2	219.789678	12.144543			
2.3	219.788568	12.142683			
2.4	219.791131	12.140390			Radial arc candidate
B1	219.7929577	12.13667192	3.48	This work, IMACS	
B2	219.7936562	12.13763932	1.53	This work, IMACS	Possible redshift, single image

Table 8
(Continued)

ID	R.A. J2000	Decl. J2000	z_{spec}	z_{spec} Reference	Notes
SDSS J1456+5702					
B.1	224.004820	57.034582	2.3660	This work, MMT	Knots in giant arc
B.2	224.002780	57.041188			
B.3	224.006960	57.034895			
Ba.1	224.008300	57.034957			
Ba.2	224.002640	57.040816			
Bb.1	224.009840	57.036207			
Bb.2	224.002320	57.041565			
Bc.1	224.000690	57.034937			
Bc.2	224.002700	57.041638			
Bd.1	223.999750	57.035006			
Bd.2	224.003040	57.041559			
Be.1	223.999940	57.034689			
Be.2	224.003390	57.041169			
Bf.1	224.010680	57.036451			
Bf.2	224.001640	57.041280			
A1	224.003905	57.042969	0.8331	Bayliss+11	Single image
A2	224.003257	57.036603	0.8324	Bayliss+11	Single image
C	224.022021	57.034751	1.1400	Bayliss+11	Single image
SDSS J1522+2535					
1.1	230.721557	25.593341	1.7096	This work, GMOS	Substructure in source 1
1.2	230.718683	25.592248			
1.3	230.717426	25.589195			
1.4	230.720750	25.590884			
1.5	230.721538	25.590773			
1a.1	230.721580	25.593523			
1a.2	230.718270	25.591888			
1a.3	230.717480	25.589447			
1a.4	230.720770	25.590667			
1b.1	230.721730	25.593499			
1b.2	230.718350	25.591777			
1b.3	230.717670	25.589403			
1b.4	230.720970	25.590605			
1 c.1	230.721800	25.592924			
1 c.2	230.719150	25.592023			
1 c.3	230.717670	25.588817			
1d.1	230.721910	25.593010			
1d.2	230.718990	25.591908			
1d.3	230.717830	25.588910			
B	230.725525	25.5879675	1.221	This work, GMOS	Possible redshift, single image
C	230.727051	25.58725537	0.973161	This work, GMOS	Single image
D	230.7270299	25.57886337	0.487957	This work, GMOS	Foreground galaxy
E	230.715947	25.57524935	0.379631	This work, GMOS	Foreground galaxy
SDSS J1527+0652					
1.1	231.938559	6.872048	2.7600	Koester+10	
1.2	231.937925	6.872142			
1.3	231.937803	6.872197			
1b.1	231.938366	6.872013			
1b.2	231.938053	6.872052			
1 c.1	231.938274	6.872022			
1 c.2	231.938162	6.872030			
1 c.3	231.937547	6.872303			
1d.1	231.938452	6.871979			
1d.2	231.937931	6.872059			
2.1	231.934215	6.877017	...	Candidate	
2.2	231.934355	6.876537			
2.3	231.934124	6.875461			

Table 8
(Continued)

ID	R.A. J2000	Decl. J2000	z_{spec}	z_{spec} Reference	Notes
3.1	231.939062	6.876848	...	Candidate	
3.2	231.939158	6.875564			
3.3	231.939727	6.874700			
4.1	231.944022	6.883274	...	Candidate	
4.2	231.945432	6.879834			
4.3	231.947061	6.877657			
5.1	231.951761	6.879191	...	Candidate	
5.2	231.951803	6.882945			
5.3	231.947973	6.886712			
6.1	231.942672	6.881764	...	Candidate	
6.2	231.943085	6.880734			

Note. Lensing constraints and other background or foreground galaxies with spectroscopic redshifts in the fields of SGAS-*HST* clusters SDSS J1343+4155, SDSS J1420+3955, SDSS J1439+1208, SDSS J1456+5702, SDSS J1522+2535, and SDSS J1527+0652. The IDs of images of lensed galaxies are labeled as *AB.X* where *A* is a number or a letter indicating the source ID (or system name); *B* is a number or a letter indicating the ID of the emission knot within the system; and *X* is a number indicating the ID of the lensed image within the multiple-image family.

References. Rigby et al. (2018b), Stark et al. (2013), Bayliss (2012), Bayliss et al. (2010, 2011b, 2014b), Kubo et al. (2010), Johnson et al. (2017b), Ofek et al. (2008), Diehl et al. (2009).

(This table is available in machine-readable form.)

Table 9
List of Lensing Constraints for Clusters Shown in Figure 6

ID	R.A. J2000	Decl. J2000	z_{spec}	z_{spec} Reference	Notes
SDSS J1531+3414					
1.1	232.79846	34.242414	1.096	Bayliss+11	
1.2	232.79147	34.241359			
1.3	232.79290	34.237469			
1.4	232.79312	34.237454			
12.1	232.79883	34.241860			
12.2	232.79204	34.241349			
13.1	232.79863	34.241870			
13.2	232.79214	34.241676			
14.1	232.79861	34.242029			
14.2	232.79197	34.241605			
15.1	232.79850	34.242660			
15.2	232.79106	34.240519			
16.1	232.79821	34.242889			
16.2	232.79379	34.237723			
17.1	232.79725	34.242966			
17.2	232.79311	34.242933			
17.3	232.79574	34.238452			
17.4	232.79018	34.239033			
2.1	232.78877	34.237850		Bayliss+11	limit: $z > 1.49$
2.2	232.79710	34.238497			
2.3	232.79809	34.243633			
2.4	232.79337	34.244258			
2a.1	232.78812	34.238060			
2a.2	232.79726	34.239392			
2b.1	232.78891	34.237212			
2b.2	232.79780	34.239135			
2b.3	232.79825	34.243064			
3.1	232.79355	34.241752		Bayliss+11	limit: >1.49
3.2	232.79224	34.235538			
D	232.7891558	34.2359015	1.026	Bayliss+11	Single image

Table 9
(Continued)

ID	R.A. J2000	Decl. J2000	z_{spec}	z_{spec} Reference	Notes
E	232.7845467	34.2413218	1.3	Bayliss+11	Single image
SDSS J1604+2244					
1.1	241.040867	22.739529	...		
1.2	241.043363	22.739298			
1.3	241.044362	22.736277			
1.4	241.041803	22.737227			
1.5	241.042247	22.737956			
A	241.047645	22.739371	1.1841	This work, GMOS	Single image
B	241.037062	22.741253	1.0333	This work, GMOS	Single image
c	241.035457	22.731761	1.6370	This work, GMOS	
d	241.047417	22.747950	0.4141	This work, GMOS	
e	241.038404	22.731987	2.0540	This work, GMOS	Low-confidence redshift
f	241.041255	22.731276	1.1843	This work, GMOS	Low-confidence redshift
g	241.041780	22.729624	1.7232	This work, GMOS	Low-confidence redshift
h	241.035411	22.732763	1.4830	This work, GMOS	Low-confidence redshift
Q	241.050890	22.734746	2.1670	SDSS DR12	QSO
SDSS J1621+0607					
A.1	245.389450	6.120616	4.1300	Bayliss+11	Ly α emitter; A1 in Bayliss+11
A.2	245.386300	6.118230			Ly α emitter; A2 in Bayliss+11
2a.1	245.385990	6.121664	1.1780	Bayliss+11	B1 in Bayliss+11
2a.2	245.386190	6.122059			
2a.3	245.385460	6.122681			
2a.4	245.382610	6.121549			
2b.3	245.385240	6.122616	1.1780	This work, LDSS3	Falls outside of the caustic of 2a.1, 2a.2
2b.4	245.382740	6.121098			
2 c.1	245.386100	6.121659			
2 c.2	245.386260	6.121953			
2 c.3	245.385360	6.122681			
2d.1	245.386200	6.121664			
2d.2	245.386310	6.121843			
2d.3	245.385288	6.122697			
2d.4	245.382710	6.121224			
C.1	245.3867270	6.125210	...	Bayliss+11	
C.2	245.3811204	6.123205			Predicted location of possible counter image
D	245.377640	6.124750	0.5066	This work, IMACS	Single image
E	245.380753	6.118075	1.31	This work, IMACS	Single image; low-confidence redshift
F	245.386307	6.123700	0.3386	This work, IMACS	Single image
SDSS J1632+3500					
1	248.047637	35.007370	1.2350	This work, GMOS	
2	248.038365	35.006802	2.2650	This work, GMOS	
3.1	248.042579	35.010737	...		Candidate
3.2	248.043008	35.011403			
4.1	248.050018	35.009041		...	Candidate
4.2	248.049811	35.007939			
5	248.041096	35.011300	0.4538	This work, GMOS	Cluster member, star-forming
6	248.043778	35.013704	0.1271	This work, GMOS	Foreground

Table 9
(Continued)

ID	R.A. J2000	Decl. J2000	z_{spec}	z_{spec} Reference	Notes
7	248.048366	35.011598	1.2318	This work, GMOS	Background, single image
SDSS J1723+3411					
1.1	260.901550	34.198336	1.3294	Kubo+10	
1.2	260.902050	34.199054			
1.3	260.901040	34.201255			
1.4	260.899850	34.199329			
1.5	260.900572	34.199449			
1a.1	260.901820	34.198623			
1a.2	260.901890	34.198710			
2.1	260.901400	34.197421	2.1650	This work, HST-GO-14230	PI: Rigby
2.2	260.902560	34.199755			
2.3	260.901040	34.201732			
2.4	260.899370	34.199521			
3.1	260.901180	34.197414	...		Assumed to be at same z as source 2
3.2	260.902500	34.199631			
3.3	260.900860	34.201795			
3.4	260.899230	34.199477			
SDSS J2111–0114					
1.1	317.827850	–1.241202	2.8580	Bayliss+11	A in Bayliss+11
1.2	317.828960	–1.242054			
1.3	317.834400	–1.242342			
1a.1	317.828530	–1.241737			
1a.2	317.828260	–1.241515			
1b.1	317.828340	–1.241774			
1b.2	317.828450	–1.241857			
1 c.1	317.828910	–1.242246			
1 c.2	317.827940	–1.241592			
1d.1	317.828700	–1.242008			
1d.2	317.828120	–1.241579			
2.1	317.833862	–1.241214	...		
2.2	317.832739	–1.241775			
3.1	317.827023	–1.241099	...		
3.2	317.830653	–1.242959			
3.3	317.833819	–1.242636			

Note. Lensing constraints and other background or foreground galaxies with spectroscopic redshifts in the fields of SGAS-*HST* clusters SDSS J1531+3414, SDSS J1604+2244, SDSS J1621+0607, SDSS J1632+3500, SDSS J1723+3411, and SDSS J2111–0114. SDSS J2243–0935. The IDs of images of lensed galaxies are labeled as $AB.X$ where A is a number or a letter indicating the source ID (or system name); B is a number or a letter indicating the ID of the emission knot within the system; and X is a number indicating the ID of the lensed image within the multiple-image family.

References. Rigby et al. (2018b), Stark et al. (2013), Bayliss (2012), Bayliss et al. (2010, 2011b, 2014b), Kubo et al. (2010), Johnson et al. (2017b), Ofek et al. (2008), Diehl et al. (2009).

(This table is available in machine-readable form.)

Table 10
List of Lensing Constraints for Clusters Shown in Figure 7

ID	R.A. J2000	Decl. J2000	z_{spec}	z_{spec} Reference	Notes
SDSS J2243–0935					
1.1	340.850935	−9.585705	2.09	A2 in Bayliss+11; Rigby+18	AGN core
1.2	340.851211	−9.586760			clumps in the host galaxy
101.1	340.851430	−9.587189			
101.2	340.851337	−9.586573			
101.3	340.851173	−9.586377			
102.1	340.851279	−9.587084			
102.2	340.851068	−9.586766			
102.3	340.851025	−9.586260			
2.1	340.858480	−9.580426	...		$z_{\text{phot}} \sim 3.0$ used as prior
2.2	340.858820	−9.581002			$z_{\text{phot}} \sim 3.0$
2.3	340.859550	−9.583349			
3.1	340.854230	−9.580533	...		
3.2	340.854490	−9.580891			
3.3	340.856975	−9.583722			
4.1	340.851790	−9.581950	...		
4.2	340.852140	−9.583397			
4.3	340.854020	−9.587714			
5.1	340.846880	−9.584385	...		
5.2	340.847240	−9.586046			
6.1	340.839270	−9.583212	...		
6.2	340.840110	−9.584314			
7.1	340.835850	−9.590120	...		
7.2	340.836190	−9.589966			
7.3	340.838472	−9.590060			
8.1	340.834010	−9.590052	...		$z_{\text{phot}} \sim 3.0$ used as prior
8.2	340.836370	−9.588974			$z_{\text{phot}} \sim 3.0$
8.3	340.839336	−9.589144			
8.4	340.835870	−9.580444			
8a.1	340.833738	−9.590145			
8a.3	340.839226	−9.589118			
8a.4	340.835763	−9.580485			
10.1	340.824680	−9.594526	...		
10.2	340.825210	−9.596464			
11.1	340.833981	−9.590439	...		
11.2	340.836653	−9.589322			
11.3	340.838693	−9.589496			
A1	340.854971	−9.581328	2.092	Bayliss+11	
B1	340.847112	−9.592340	1.3202	Bayliss+11	Single image
C1	340.851833	−9.596300	0.7403	Bayliss+11	Single image
D	340.852299	−9.604503912	0.79	This work, IMACS	Galaxy–Galaxy lensing
E	340.8573348	−9.57659422	3.378	This work, IMACS	Galaxy–Galaxy lensing

Note. Lensing constraints and other background or foreground galaxies with spectroscopic redshifts in the fields of SGAS-*HST* cluster SDSS J2243–0935. The IDs of images of lensed galaxies are labeled as $AB.X$ where A is a number or a letter indicating the source ID (or system name); B is a number or a letter indicating the ID of the emission knot within the system; and X is a number indicating the ID of the lensed image within the multiple-image family.

References. Rigby et al. (2018b), Stark et al. (2013), Bayliss (2012), Bayliss et al. (2010, 2011b, 2014b), Kubo et al. (2010), Johnson et al. (2017b), Ofek et al. (2008), Diehl et al. (2009).

(This table is available in machine-readable form.)

Appendix B

Spectroscopy Catalog

Table 11 provides the spectroscopic redshifts of cluster-member galaxies that were measured in this work, from the literature, and from the SDSS. The spectroscopic redshifts of non-cluster members are given in Appendix A.

Table 11
List of Spectroscopic Redshifts

Cluster	R.A. J2000	Decl. J2000	z	Reference
SDSS J0928+2031	09:28:06.668	+20:32:06.46	0.1932	Gemini/GMOS-GN15AQ38
	09:28:04.818	+20:31:46.84	0.1872	Gemini/GMOS-GN15AQ38
	09:28:03.098	+20:31:25.64	0.1988	Gemini/GMOS-GN15AQ38
	09:28:04.928	+20:31:29.24	0.1851	Gemini/GMOS-GN15AQ38
	09:28:10.617	+20:31:52.38	0.1893	Gemini/GMOS-GN15AQ38
	09:28:10.325	+20:31:42.66	0.1935	Gemini/GMOS-GN15AQ38
	09:28:07.084	+20:31:20.02	0.1920	Gemini/GMOS-GN15AQ38
	09:28:14.500	+20:31:44.04	0.1885	Gemini/GMOS-GN15AQ38
	09:28:06.301	+20:30:57.09	0.1915	Gemini/GMOS-GN15AQ38
	09:28:02.236	+20:30:34.59	0.1893	Gemini/GMOS-GN15AQ38
	09:28:04.629	+20:30:44.78	0.1906	Gemini/GMOS-GN15AQ38
	09:28:13.988	+20:31:24.52	0.1949	Gemini/GMOS-GN15AQ38
	09:28:08.272	+20:30:51.62	0.1954	Gemini/GMOS-GN15AQ38
	09:28:07.468	+20:30:22.92	0.1904	Gemini/GMOS-GN15AQ38
	09:28:04.962	+20:30:06.18	0.1978	SDSS DR12
	09:28:04.534	+20:31:45.15	0.1920	SDSS DR12
	09:28:13.826	+20:30:43.65	0.1897	SDSS DR12
	09:28:22.205	+20:29:10.13	0.1972	SDSS DR12
	09:27:47.657	+20:33:34.87	0.1935	SDSS DR12
SDSS J0952+3434	09:52:40.222	+34:34:46.07	0.3597	SDSS DR12
	09:52:41.616	+34:34:14.08	0.3570	SDSS DR12
	09:52:41.693	+34:36:03.10	0.3529	Gemini/GMOS-GN15BQ26
	09:52:38.978	+34:35:54.77	0.3594	Gemini/GMOS-GN15BQ26
	09:52:35.313	+34:35:39.75	0.3580	Gemini/GMOS-GN15BQ26
	09:52:37.398	+34:34:57.64	0.3553	Gemini/GMOS-GN15BQ26
	09:52:40.756	+34:34:14.84	0.3616	Gemini/GMOS-GN15BQ26
	09:52:43.880	+34:34:17.73	0.3542	Gemini/GMOS-GN15BQ26
	09:52:40.352	+34:34:06.46	0.3532	Gemini/GMOS-GN15BQ26
	09:52:46.453	+34:33:52.97	0.3594	Gemini/GMOS-GN15BQ26
SDSS J1002+2031	10:02:26.832	+20:31:01.92	0.3205	SDSS DR12
	10:02:14.136	+20:32:16.44	0.3196	SDSS DR12
	10:02:28.776	+20:29:05.64	0.3168	SDSS DR12
	10:02:44.880	+20:29:29.40	0.3085	SDSS DR12
	10:02:45.072	+20:31:02.28	0.3136	SDSS DR12
	10:02:11.136	+20:32:15.00	0.3187	SDSS DR12
	10:02:38.496	+20:28:01.20	0.3215	SDSS DR12
	10:02:44.568	+20:31:33.24	0.3305	SDSS DR12
	10:02:42.696	+20:30:36.72	0.3194	SDSS DR12
	10:02:28.392	+20:31:01.01	0.3194	Gemini/GMOS-GN15BQ26
	10:02:28.422	+20:30:06.54	0.3152	Gemini/GMOS-GN15BQ26
	10:02:28.289	+20:31:07.35	0.3245	Gemini/GMOS-GN15BQ26
	10:02:25.264	+20:30:56.94	0.3175	Gemini/GMOS-GN15BQ26
	10:02:28.000	+20:30:34.04	0.3217	Gemini/GMOS-GN15BQ26
	10:02:26.400	+20:30:30.59	0.3191	Gemini/GMOS-GN15BQ26
	10:02:30.695	+20:30:50.14	0.3188	Gemini/GMOS-GN15BQ26
	10:02:28.309	+20:31:43.74	0.3206	Gemini/GMOS-GN15BQ26
	10:02:25.981	+20:31:48.60	0.3230	Gemini/GMOS-GN15BQ26
	10:02:28.419	+20:31:11.49	0.3157	Gemini/GMOS-GN15BQ26
	10:02:26.737	+20:31:30.17	0.3093	Gemini/GMOS-GN15BQ26
	10:02:23.262	+20:30:39.73	0.3235	Gemini/GMOS-GN11AQ19

Table 11
(Continued)

Cluster	R.A. J2000	Decl. J2000	z	Reference
SDSS J1522+2535	10:02:25.964	+20:30:44.26	0.3153	Gemini/GMOS-GN11AQ19
	10:02:16.879	+20:30:54.20	0.3275	Gemini/GMOS-GN11AQ19
	10:02:30.479	+20:30:16.83	0.3126	Gemini/GMOS-GN11AQ19
	10:02:25.463	+20:30:20.32	0.3223	Gemini/GMOS-GN11AQ19
	10:02:24.617	+20:31:28.95	0.3226	Gemini/GMOS-GN11AQ19
	10:02:23.503	+20:30:34.47	0.3238	Gemini/GMOS-GN11AQ19
	10:02:27.478	+20:30:47.82	0.3197	Gemini/GMOS-GN11AQ19
	10:02:26.909	+20:30:51.14	0.3143	Gemini/GMOS-GN11AQ19
	10:02:23.774	+20:30:55.46	0.3195	Gemini/GMOS-GN11AQ19
	10:02:25.971	+20:31:01.83	0.3114	Gemini/GMOS-GN11AQ19
	10:02:28.756	+20:31:10.58	0.3139	Gemini/GMOS-GN11AQ19
	10:02:25.012	+20:32:09.34	0.3157	Gemini/GMOS-GN11AQ19
	10:02:25.394	+20:31:15.98	0.3189	Gemini/GMOS-GN11AQ19
	10:02:30.050	+20:31:23.90	0.3151	Gemini/GMOS-GN11AQ19
SDSS J1621+0607	10:02:32.663	+20:31:26.31	0.3228	Gemini/GMOS-GN11AQ19
	10:02:22.687	+20:32:24.04	0.3120	Gemini/GMOS-GN11AQ19
	15:22:53.524	+25:36:40.27	0.6042	SDSS DR12
	15:22:50.681	+25:33:34.58	0.5917	SDSS DR12
	15:22:45.102	+25:36:56.98	0.6013	Gemini/GMOS MOS
	15:22:51.614	+25:35:24.96	0.6046	Gemini/GMOS MOS
	15:22:51.900	+25:35:04.95	0.5885	Gemini/GMOS MOS
	15:22:52.528	+25:34:36.23	0.6071	Gemini/GMOS MOS
	15:22:52.686	+25:34:46.52	0.5995	Gemini/GMOS MOS
	15:22:52.802	+25:36:01.37	0.6023	Gemini/GMOS MOS
	15:22:53.304	+25:35:54.81	0.5928	Gemini/GMOS MOS
	15:22:53.536	+25:36:40.13	0.6043	Gemini/GMOS MOS
	15:22:54.162	+25:34:25.91	0.6031	Gemini/GMOS MOS
	15:22:54.285	+25:34:24.15	0.6060	Gemini/GMOS MOS
	15:22:54.313	+25:35:24.39	0.6090	Gemini/GMOS MOS
	15:22:54.880	+25:35:17.59	0.6088	Gemini/GMOS MOS
SDSS J1621+0607	16:21:32.746	+06:07:10.97	0.3382	Bayliss et al. (2011b)
	16:21:32.731	+06:07:13.82	0.3390	Bayliss et al. (2011b)
	16:21:28.469	+06:06:52.97	0.3437	Bayliss et al. (2011b)
	16:21:33.158	+06:07:26.67	0.3408	Bayliss et al. (2011b)
	16:21:33.965	+06:07:23.35	0.3420	Bayliss et al. (2011b)
	16:21:31.694	+06:07:44.14	0.3406	Bayliss et al. (2011b)
	16:21:31.966	+06:07:48.24	0.3436	Bayliss et al. (2011b)
	16:21:35.638	+06:06:28.89	0.3367	Bayliss et al. (2011b)
	16:21:33.394	+06:07:13.93	0.3505	Bayliss et al. (2011b)
	16:21:32.830	+06:07:24.31	0.3391	Bayliss et al. (2011b)
	16:21:32.698	+06:07:28.43	0.3522	Bayliss et al. (2011b)
	16:21:16.227	+06:10:59.42	0.3446	Magellan/IMACS MOS
	16:21:16.797	+06:18:32.11	0.3037	Magellan/IMACS MOS
	16:21:18.122	+06:13:58.32	0.3185	Magellan/IMACS MOS
	16:21:19.303	+06:14:39.07	0.3008	Magellan/IMACS MOS
	16:21:22.008	+06:08:20.09	0.3000	Magellan/IMACS MOS
	16:21:22.420	+06:01:29.46	0.3397	Magellan/IMACS MOS
	16:21:25.778	+06:02:09.85	0.3412	Magellan/IMACS MOS
	16:21:26.176	+06:08:35.22	0.3421	Magellan/IMACS MOS
	16:21:36.517	+06:04:07.66	0.3214	Magellan/IMACS MOS
	16:21:36.970	+06:06:58.79	0.3433	Magellan/IMACS MOS
	16:21:39.339	+06:02:01.51	0.3415	Magellan/IMACS MOS
	16:21:39.669	+05:59:52.43	0.3161	Magellan/IMACS MOS
	16:21:41.159	+06:02:16.98	0.3446	Magellan/IMACS MOS
	16:21:43.658	+06:07:30.44	0.3412	Magellan/IMACS MOS
	16:21:43.672	+06:03:43.78	0.3001	Magellan/IMACS MOS
	16:21:43.947	+06:00:40.68	0.3402	Magellan/IMACS MOS
	16:21:46.199	+06:02:55.47	0.3460	Magellan/IMACS MOS
	16:21:46.831	+06:03:13.22	0.3436	Magellan/IMACS MOS

Table 11
(Continued)

Cluster	R.A. J2000	Decl. J2000	z	Reference
	16:21:49.248	+06:02:57.76	0.3439	<i>Magellan</i> /IMACS MOS
	16:21:53.388	+06:04:56.83	0.3385	<i>Magellan</i> /IMACS MOS
	16:21:55.331	+06:06:01.89	0.3418	<i>Magellan</i> /IMACS MOS
	16:21:56.464	+06:14:45.48	0.3318	<i>Magellan</i> /IMACS MOS
	16:21:56.533	+06:07:44.87	0.3963	<i>Magellan</i> /IMACS MOS
	16:21:59.376	+06:16:36.90	0.3461	<i>Magellan</i> /IMACS MOS
	16:22:02.466	+05:59:54.13	0.3446	<i>Magellan</i> /IMACS MOS
	16:22:11.728	+05:59:43.15	0.3490	<i>Magellan</i> /IMACS MOS
	16:22:19.007	+06:14:34.83	0.3412	<i>Magellan</i> /IMACS MOS
	16:21:32.746	+06:07:10.97	0.3412	<i>Magellan</i> /IMACS MOS
	16:21:32.731	+06:07:13.82	0.3436	<i>Magellan</i> /IMACS MOS
	16:21:28.469	+06:06:52.97	0.3412	<i>Magellan</i> /IMACS MOS
	16:21:33.158	+06:07:26.67	0.3392	<i>Magellan</i> /IMACS MOS
	16:21:33.965	+06:07:23.35	0.3434	<i>Magellan</i> /IMACS MOS
	16:21:31.694	+06:07:44.14	0.3392	<i>Magellan</i> /IMACS MOS
	16:21:31.966	+06:07:48.24	0.3441	<i>Magellan</i> /IMACS MOS
	16:21:35.638	+06:06:28.89	0.3435	<i>Magellan</i> /IMACS MOS
	16:21:33.394	+06:07:13.93	0.3320	<i>Magellan</i> /IMACS MOS
	16:21:32.830	+06:07:24.31	0.3326	<i>Magellan</i> /IMACS MOS
	16:21:32.698	+06:07:28.43	0.3443	<i>Magellan</i> /IMACS MOS
SDSS J1632+3500	16:32:07.962	+35:00:46.950	0.467806	Gemini/GMOS-GN11AQ19
	16:32:08.188	+35:00:12.340	0.459047	Gemini/GMOS-GN11AQ19
	16:32:12.515	+34:59:54.832	0.464104	Gemini/GMOS-GN11AQ19
	16:32:07.433	+35:00:25.044	0.471901	Gemini/GMOS-GN11AQ19
	16:32:04.769	+35:01:01.796	0.465734	Gemini/GMOS-GN11AQ19
	16:32:09.859	+35:00:40.741	0.453848	Gemini/GMOS-GN11AQ19; star-forming
	16:32:14.773	+35:00:24.579	0.471658	Gemini/GMOS-GN11AQ19
	16:32:02.585	+35:01:43.225	0.469637	Gemini/GMOS-GN11AQ19
	16:32:16.188	+35:00:41.964	0.463060	Gemini/GMOS-GN11AQ19
	16:31:55.872	+35:00:10.084	0.471787	SDSS DR12
	16:32:08.117	+35:00:32.674	0.470646	SDSS DR12

Note. Spectroscopic redshifts of cluster-member galaxies.

ORCID iDs

Keren Sharon  <https://orcid.org/0000-0002-7559-0864>
 Matthew B. Bayliss  <https://orcid.org/0000-0003-1074-4807>
 Håkon Dahle  <https://orcid.org/0000-0003-2200-5606>
 Samuel J. Dunham  <https://orcid.org/0000-0003-4008-6438>
 Michael K. Florian  <https://orcid.org/0000-0001-5097-6755>
 Michael D. Gladders  <https://orcid.org/0000-0003-1370-5010>
 Traci L. Johnson  <https://orcid.org/0000-0002-8829-5303>
 Guillaume Mahler  <https://orcid.org/0000-0003-3266-2001>
 Rachel Paterno-Mahler  <https://orcid.org/0000-0003-3653-3741>
 Jane R. Rigby  <https://orcid.org/0000-0002-7627-6551>
 Katherine E. Whitaker  <https://orcid.org/0000-0001-7160-3632>
 Mohammad Akhshik  <https://orcid.org/0000-0002-3240-7660>
 Juan David Remolina González  <https://orcid.org/0000-0002-7868-9827>
 Eva Wuyts  <https://orcid.org/0000-0002-4105-3315>

References

- Abazajian, K. N., Adelman-McCarthy, J. K., Agüeros, M. A., et al. 2009, *ApJS*, **182**, 543
 Acebron, A., Jullo, E., Limousin, M., et al. 2017, *MNRAS*, **470**, 1809
 Bai, L., Marcillac, D., Rieke, G. H., et al. 2007, *ApJ*, **664**, 181
 Bayliss, M. B. 2012, *ApJ*, **744**, 156
 Bayliss, M. B., Gladders, M. D., Oguri, M., et al. 2011a, *ApJL*, **727**, L26
 Bayliss, M. B., Hennawi, J. F., Gladders, M. D., et al. 2011b, *ApJS*, **193**, 8
 Bayliss, M. B., Johnson, T., Gladders, M. D., Sharon, K., & Oguri, M. 2014a, *ApJ*, **783**, 41
 Bayliss, M. B., Rigby, J. R., Sharon, K., et al. 2014b, *ApJ*, **790**, 144
 Bayliss, M. B., Wuyts, E., Sharon, K., et al. 2010, *ApJ*, **720**, 1559
 Beers, T. C., Flynn, K., & Gebhardt, K. 1990, *AJ*, **100**, 32
 Bertin, E., & Arnouts, S. 1996, *A&AS*, **117**, 393
 Blanchard, P. K., Bayliss, M. B., McDonald, M., et al. 2013, *ApJ*, **772**, 24
 Blanton, M. R., Bershad, M. A., Abolfathi, B., et al. 2017, *AJ*, **154**, 28
 Brammer, G. B., van Dokkum, P. G., & Coppi, P. 2008, *ApJ*, **686**, 1503
 Broadhurst, T., Benítez, N., Coe, D., et al. 2005, *ApJ*, **621**, 53
 Butcher, H., & Oemler, A., Jr. 1978, *ApJ*, **219**, 18
 Butcher, H., & Oemler, A., Jr. 1984, *ApJ*, **285**, 426
 Cabanac, R. A., Valls-Gabaud, D., & Lidman, C. 2008, *MNRAS*, **386**, 2065
 Cain, B., Bradač, M., & Levinson, R. 2016, *MNRAS*, **463**, 4287
 Carrasco, M., Barrientos, L. F., Anguita, T., et al. 2017, *ApJ*, **834**, 210
 Cerny, C., Sharon, K., Andrade-Santos, F., et al. 2018, *ApJ*, **859**, 159
 Chisholm, J., Gazagnes, S., Schaerer, D., et al. 2018, *A&A*, **616**, A30
 Coe, D., Zitrin, A., Carrasco, M., et al. 2013, *ApJ*, **762**, 32
 Cooke, K. C., O'Dea, C. P., Baum, S. A., et al. 2016, *ApJ*, **833**, 224
 Dahle, H., Gladders, M. D., Sharon, K., et al. 2013, *ApJ*, **773**, 146
 Dahle, H., Gladders, M. D., Sharon, K., Bayliss, M. B., & Rigby, J. R. 2015, *ApJ*, **813**, 67
 Dessauges-Zavadsky, M., Christensen, L., D'Odorico, S., Schaerer, D., & Richard, J. 2011, *A&A*, **533**, A15
 Diehl, H. T., Allam, S. S., Annis, J., et al. 2009, *ApJ*, **707**, 686

- Ebeling, H., Edge, A. C., Mantz, A., et al. 2010, *MNRAS*, **407**, 83
- Ebeling, H., Stephenson, L. N., & Edge, A. C. 2014, *ApJL*, **781**, L40
- Elíasdóttir, Á., Limousin, M., Richard, J., et al. 2007, arXiv:0710.5636
- Evrard, A. E., Bialek, J., Busha, M., et al. 2008, *ApJ*, **672**, 122
- Fairley, B. W., Jones, L. R., Wake, D. A., et al. 2002, *MNRAS*, **330**, 755
- Gal-Yam, A., Maoz, D., Guhathakurta, P., & Filippenko, A. V. 2003, *AJ*, **125**, 1087
- Gal-Yam, A., Maoz, D., & Sharon, K. 2002, *MNRAS*, **332**, 37
- Gladders, M. D., Rigby, J. R., Sharon, K., et al. 2013, *ApJ*, **764**, 177
- Gladders, M. D., & Yee, H. K. C. 2000, *AJ*, **120**, 2148
- Gonzaga, S., Hack, W., Fruchter, A., et al. 2012, The DrizzlePac Handbook (Baltimore, MD: STScI)
- Gralla, M. B., Sharon, K., Gladders, M. D., et al. 2011, *ApJ*, **737**, 74
- Hansen, S. M., Sheldon, E. S., Wechsler, R. H., & Koester, B. P. 2009, *ApJ*, **699**, 1333
- Hashimoto, T., Laporte, N., Mawatari, K., et al. 2018, *Natur*, **557**, 392
- Hennawi, J. F., Gladders, M. D., Oguri, M., et al. 2008, *AJ*, **135**, 664
- Hook, I. M., Jørgensen, I., Allington-Smith, J. R., et al. 2004, *PASP*, **116**, 425
- Irwin, J. A., Dupke, R., Carrasco, E. R., et al. 2015, *ApJ*, **806**, 268
- Johnson, T. L., Rigby, J. R., Sharon, K., et al. 2017a, *ApJL*, **843**, L21
- Johnson, T. L., & Sharon, K. 2016, *ApJ*, **832**, 82
- Johnson, T. L., Sharon, K., Bayliss, M. B., et al. 2014, *ApJ*, **797**, 48
- Johnson, T. L., Sharon, K., Gladders, M. D., et al. 2017b, *ApJ*, **843**, 78
- Jullo, E., & Kneib, J.-P. 2009, *MNRAS*, **395**, 1319
- Jullo, E., Kneib, J.-P., Limousin, M., et al. 2007, *NJPh*, **9**, 447
- Kimble, R. A., MacKenty, J. W., O'Connell, R. W., & Townsend, J. A. 2008, *Proc. SPIE*, **7010**, 70101E
- Koester, B. P., Gladders, M. D., Hennawi, J. F., et al. 2010, *ApJL*, **723**, L73
- Koester, B. P., McKay, T. A., Annis, J., et al. 2007, *ApJ*, **660**, 221
- Kubo, J. M., Allam, S. S., Drabek, E., et al. 2010, *ApJL*, **724**, L137
- Limousin, M., Kneib, J.-P., & Natarajan, P. 2005, *MNRAS*, **356**, 309
- Loh, Y.-S., Ellingson, E., Yee, H. K. C., et al. 2008, *ApJ*, **680**, 214
- Madau, P., & Dickinson, M. 2014, *ARA&A*, **52**, 415
- McPartland, C., Ebeling, H., Roediger, E., & Blumenthal, K. 2016, *MNRAS*, **455**, 2994
- Meneghetti, M., Natarajan, P., Coe, D., et al. 2017, *MNRAS*, **472**, 3177
- Merten, J., Meneghetti, M., Postman, M., et al. 2015, *ApJ*, **806**, 4
- Ofek, E. O. 2014, MATLAB package for astronomy and astrophysics, Astrophysics Source Code Library, ascl:1407.005
- Ofek, E. O., Seitz, S., & Klein, F. 2008, *MNRAS*, **389**, 311
- Oguri, M., Bayliss, M. B., Dahle, H., et al. 2012, *MNRAS*, **420**, 3213
- Peng, C. Y., Ho, L. C., Impey, C. D., & Rix, H.-W. 2010, *AJ*, **139**, 2097
- Pettini, M., Rix, S. A., Steidel, C. C., et al. 2002, *ApJ*, **569**, 742
- Pettini, M., Steidel, C. C., Adelberger, K. L., Dickinson, M., & Giavalisco, M. 2000, *ApJ*, **528**, 96
- Porter, S. C., Raychaudhury, S., Pimbblet, K. A., & Drinkwater, M. J. 2008, *MNRAS*, **388**, 1152
- Priewe, J., Williams, L. L. R., Liesenborgs, J., Coe, D., & Rodney, S. A. 2017, *MNRAS*, **465**, 1030
- Quider, A. M., Pettini, M., Shapley, A. E., & Steidel, C. C. 2009, *MNRAS*, **398**, 1263
- Quider, A. M., Shapley, A. E., Pettini, M., Steidel, C. C., & Stark, D. P. 2010, *MNRAS*, **402**, 1467
- Rajan, A. 2010, WFC3 Data Handbook, v2.1 (Baltimore, MD: STScI)
- Rigby, J. R., Bayliss, M. B., Chisholm, J., et al. 2018a, *ApJ*, **853**, 87
- Rigby, J. R., Bayliss, M. B., Gladders, M. D., et al. 2014, *ApJ*, **790**, 44
- Rigby, J. R., Bayliss, M. B., Gladders, M. D., et al. 2015, *ApJL*, **814**, L6
- Rigby, J. R., Bayliss, M. B., Sharon, K., et al. 2018b, *AJ*, **155**, 104
- Rigby, J. R., Johnson, T. L., Sharon, K., et al. 2017, *ApJ*, **843**, 79
- Rigby, J. R., Wuyts, E., Gladders, M. D., Sharon, K., & Becker, G. D. 2011, *ApJ*, **732**, 59
- Ruel, J., Bazin, G., Bayliss, M., et al. 2014, *ApJ*, **792**, 45
- Saintonge, A., Tran, K.-V. H., & Holden, B. P. 2008, *ApJL*, **685**, L113
- Salmon, B., Coe, D., Bradley, L., et al. 2018, *ApJL*, **864**, L22
- Sand, D. J., Graham, M. L., Bildfell, C., et al. 2011, *ApJ*, **729**, 142
- Schirmer, M., Hildebrandt, H., Kuijken, K., & Erben, T. 2011, *A&A*, **532**, A57
- Sharon, K., Bayliss, M. B., Dahle, H., et al. 2017, *ApJ*, **835**, 5
- Sharon, K., Gal-Yam, A., Maoz, D., et al. 2010, *ApJ*, **718**, 876
- Sharon, K., Gladders, M. D., Marrone, D. P., et al. 2015, *ApJ*, **814**, 21
- Sharon, K., Gladders, M. D., Rigby, J. R., et al. 2014, *ApJ*, **795**, 50
- Sharon, K., & Johnson, T. L. 2015, *ApJL*, **800**, L26
- Smith, G. P., Ebeling, H., Limousin, M., et al. 2009, *ApJL*, **707**, L163
- Stark, D. P., Auger, M., Belokurov, V., et al. 2013, *MNRAS*, **436**, 1040
- Sun, M., Donahue, M., Roediger, E., et al. 2010, *ApJ*, **708**, 946
- Watson, D., Christensen, L., Knudsen, K. K., et al. 2015, *Natur*, **519**, 327
- Whitaker, K. E., Labbé, I., van Dokkum, P. G., et al. 2011, *ApJ*, **735**, 86
- Whitaker, K. E., Rigby, J. R., Brammer, G. B., et al. 2014, *ApJ*, **790**, 143
- Wuyts, E., Rigby, J. R., Gladders, M. D., et al. 2012a, *ApJ*, **745**, 86
- Wuyts, E., Rigby, J. R., Sharon, K., & Gladders, M. D. 2012b, *ApJ*, **755**, 73
- Zheng, W., Postman, M., Zitrin, A., et al. 2012, *Natur*, **489**, 406
- Zitrin, A., Fabris, A., Merten, J., et al. 2015, *ApJ*, **801**, 44
- Zitrin, A., Zheng, W., Broadhurst, T., et al. 2014, *ApJL*, **793**, L12